Ship evacuation simulation using a game engine: Modelling, testing and validation

Gabriele Montecchiari, Gabriele Bulian * and Paolo Gallina
Department of Engineering and Architecture, University of Trieste, Trieste, Italy

Accepted 4 January 2022

The topic of evacuation analysis plays an important role in the maritime field, because of its natural link to safety and also because of relevant SOLAS requirements. In this context, this paper focuses on the description, testing and validation of an agent-based mathematical model. As primary goal, the model has been developed targeting a use in evacuation simulations using immersive virtual reality, also with the possibility of real-time human participation. At the same time, the model is suitable also for standard evacuation simulations. The model has been developed starting from existing social force models and introducing a series of improvements, modifications, new modelling, and adaptations. The model is described in detail, providing and discussing all adopted parameters. The choice of a game engine as development environment is also discussed, highlighting benefits and limitations. Results from IMO test cases, validations using experimental data, and comparisons with FDS+Evac are presented. A more realistic test case, relevant to the maritime field, with a two-cabin-deck geometry is also presented, together with corresponding simulation results. Particular attention is paid to the post-processing and reporting of the results from Monte Carlo simulations, in order to properly reflect, quantify and emphasize the underlying aleatory uncertainty.

Keywords: Agent-based simulation, evacuation, IMO, passenger ships, social force model

1. Introduction

In the operational life of a vessel there might be unfortunate cases of emergencies, such as flooding and fire, which could require the abandonment of the ship. In the maritime sector, the assessment of the ship layout from the point of view of evacuation is particularly important in case of vessels carrying a large number of people on-board. The International Maritime Organization (IMO) already recognized, in the past, the importance of evacuation analysis, particularly in case of ro-ro passenger

*Corresponding author: Gabriele Bulian, Department of Engineering and Architecture, University of Trieste, Building C5, Floor II, Via A. Valerio, 10, 34127 Trieste, Italy. E-mail: gbulian@units.it; Tel.: +39-040-5583444.

ships. Following the entering into force of SOLAS amendment in MSC.404(96) [31], evacuation analysis for the evaluation of escape routes, early in the design process, is presently mandatory for ro-ro passenger vessels constructed on or after 1 July 1999, and for other passenger ships constructed on or after 1 January 2020 and carrying more than 36 passengers (see SOLAS/II-2/D/13 [33]). In parallel, the IMO Maritime Safety Committee also approved the revised guidelines on evacuation analysis for new and existing passenger ships, which are available as MSC.1/Circ.1533 [32].

According to MSC.1/Circ.1533 [32], two methods can be used for the evacuation analysis: a "simplified" one and an "advanced" one. The simplified evacuation analysis is based, fundamentally, on a so-called "macroscopic" type of modelling for the crowd behaviour, based on the evidence that crowds can be approximately modelled by approaches borrowed from fluid-dynamics (e.g. [28,30,36,37]). Instead, the advanced evacuation analysis is expected to make use of so-called "agent based" models (in a "mesoscopic" or "microscopic" framework). Agent-based approaches model the dynamics of each single pedestrian (an "agent") and allow the control of each single agent in terms of properties and behaviour, as required by the IMO guidelines. As a result, agent-based approaches allow considering the heterogeneity of the population and obtaining information concerning the state of each single pedestrian (an "agent") at each time instant during the simulation.

Different agent-based evacuation simulation tools have been developed in the past, with some of them specifically targeting the maritime field. An example list of some tools for evacuation analysis is reported in Table 1, indicating also those models that have been originally developed specifically for application in the maritime field. More extensive lists are given by, e.g., Deere [4] and Montecchiari [47].

Various classifications of evacuation models and corresponding evacuation tools have been proposed in literature (e.g. [9,71,79]). One major differentiation between different models can be identified in the space representation. In models such as cellular automata (e.g. [19,64]) agents can occupy a discrete set of positions, whereas in models such as the social force (e.g. [23,45]) and velocity based models (e.g. [6,8,

Table 1
Examples of evacuation simulation tools

Name	References	Space representation
AENEAS/PedGo*	[46,69]	Discrete
EvacSim	[51]	Hybrid
EVI*	[17,70]	Hybrid
FDS+Evac	[25,40]	Continuous
VELOS*	[14,15]	Continuous
VISSIM/VISWALK	[29,58]	Continuous
STEPS	[66,72]	Discrete
SIMPEV*	[19,55]	Discrete
MaritimeEXODUS*	[10,12]	Discrete

* Specifically developed for maritime field.

60]) the set of agents possible positions is continuous. Models based on continuous space are computationally more expensive, but are generally more realistic and more flexible. Table 1 provides information on the space representation for the reported example tools, and "hybrid" indicates a space representation that combines elements of continuous and discrete approaches.

While single agent-based tools can significantly differ in their underlying mathematical model, they are typically characterised by being stochastic. Therefore, the simulation output must be analysed in the ensemble domain, and Monte Carlo simulations are often implemented for this purpose. As a result, it is fundamental that simulation results are analysed by properly addressing, quantifying and reporting the aleatory (or irreducible) uncertainty of the model, i.e. that part of uncertainty which is intrinsic to the modelled phenomenon. In principle, it would be worth taking into account also epistemic (or reducible) uncertainty (e.g. [7,27]), i.e. that part of uncertainty, related to the modelling itself, which could potentially be reduced by increasing the knowledge of the system (e.g. by gathering more data or improving the model itself), although this is often a conceptually more complex and subtle subject which goes beyond the scope of this paper. The correct representation of uncertainty is fundamental especially when simulation outcomes are compared to experimental data for validation or calibration purposes, and in this case the uncertainties related to the experimental data should also be quantified and considered in the comparison.

Validation, in particular, is an important and complex step in the development of a mathematical model for engineering purposes. Results from simulations and experiments can be compared on a qualitative (see, e.g. [64]) or a quantitative basis. The IMO test cases in MSC.1/Circ.1533 [32] represent a mostly qualitative type of validation. Unfortunately, performing human evacuation experiments is difficult, and assessment of associated aleatory uncertainty is especially difficult. Therefore, the availability of highly controlled validation data sets in literature is limited (e.g. [35,44]). For the model presented herein, example quantitative validation based on real experiments has been reported by Santos et al. [63].

In particular, few validation data sets are specifically related to the maritime field. A valuable unique contribution in this respect has been produced during the project SAFEGUARD [62], where full-scale evacuation trials were performed on a ro-ro passenger ship and on a large cruise vessel. Resulting data have been reported by Deere et al. [5], Galea et al. [11] and Brown et al. [1].

From an application perspective, models used for advanced evacuation analysis in the maritime field are typically run in batch mode, without any real-time user participation, with VELOS [14,15] being a notable exception. Giving, instead, the possibility for a user to interact with the simulation in real-time, through immersive virtual reality, can give the opportunity to explore new uses of evacuation simulations for design, for training of passengers and crew, and also for the development and calibration of mathematical models. In this latter respect, in fact, results by Moussaïd et al. [50] and Olivier et al. [53] indicate that virtual reality experiments, which are

highly controllable, have potential for being used as a complementary information to real world data.

Considering the importance of evacuation from a safety perspective, the described potentialities of virtual reality, and the importance of using validated tools, it is therefore deemed useful to pursue the development of an evacuation tool which can potentially allow real-time human participation and which is also verified and validated. This paper, therefore, presents the phase of such an activity that is specifically aimed at the development, verification and validation of the agent-based mathematical model governing the evacuation process. A subsequent phase of the research then aimed at exploiting the tool capabilities regarding virtual reality and real-time human interaction [47–49].

From the point of view of modelling, Helbing and Molnar [23] introduced the social force model to describe pedestrian behaviour. The social force model simulates pedestrian dynamics by treating agents as rigid bodies that are forced by interaction and motive forces. This social force model can reproduce most of the observed patterns of crowd behaviour, also in panic conditions, as reported by Helbing et al. [21]. Different modifications of this social force model have been proposed in the past in order to add the possibility to simulate specific human behaviours, e.g. Xi et al. [74] model group behaviour and vision field, Johansson et al. [39] model waiting behaviour, Qu et al. [59] model the behaviour on stairs. A notable modified version of the original social force model by Helbing and Molnar [23] has been developed and implemented in the FDS+Evac evacuation simulation tool [40]. The social force model represents the basis also for the modelling presented in this work.

In the following, firstly, the model is summarised, while details of the implemented mathematical model are described in the Appendix, providing and discussing all the adopted parameters. The model is based on the social force approach by Helbing and Molnar [23] and it represents a modification of the FDS+Evac modelling [40]. The reference starting models have been modified in a series of aspects, to introduce some improvements, where deemed appropriate, to make the model better suited for applications targeting real-time human participation and to better adapt the model to the used development environment. The mathematical model is described in detail for two main reasons: to allow reproducibility and because, during the present study, it was observed that modelling details can have an impact on simulations outcomes. After the description of the mathematical model, the choice of the development environment, the Unity3D game engine [67], is discussed, highlighting benefits and limitations. Then, test results are reported together with comparisons with results obtained by the software FDS+Evac [40] and/or with experimental data [76,78], for testing and validation purpose. Particular attention is paid to reporting results by quantifying the associated aleatory uncertainty, providing, therefore, useful additional information regarding the distributions of the analysed characteristics. A new test case, targeting specifically the maritime field and derived from the cruise vessel data from the SAFEGUARD project [62], is finally described, and simulation outcomes are reported and commented. Scope of this proposed test case is to have

a geometry which is sufficiently representative of a realistic ship geometry, while still being sufficiently simple for being implemented also in case of early software development and when testing different tools/mathematical models. All results are reported in detail, in order to facilitate possible comparisons by other researchers using different tools. Concluding remarks are finally provided. It is noted that this work provides information on part of a more extensive development that has been thoroughly described by Montecchiari [47].

2. Mathematical modelling

The simulation approach presented herein is based on the social force model. In particular, the social force-based model was implemented starting from Helbing and Molnar [23] and from the model embedded in FDS+Evac [40]. However, the reference starting models have been modified in a series of aspects, to introduce some improvements, where deemed appropriate, to make the model better suited for applications targeting real-time human participation and to better adapt the model to the used development environment.

Details regarding the modelling are provided in the Appendix, and this section is intended to report some essential aspects.

Basically, the reference social force modelling describes the dynamics of each agent as that of a rigid body with three degrees of freedom, i.e. two planar translations and one rotation. The dynamics of each agent is governed by rigid body dynamics laws, i.e.

$$\begin{cases} m_i \cdot \ddot{\mathbf{x}}_i(t) = \mathbf{F}_i^g(t) \\ I_{z,i} \cdot \ddot{\phi}_i(t) = T_i^g(t) \end{cases} \tag{1}$$

where m_i (kg) is the mass of the ith agent, $\mathbf{x}_i(t)$ (m) is its instantaneous two-dimensional position vector, $\mathbf{F}_i^g(t)$ (N) is the global instantaneous force vector acting on the ith agent, $I_{z,i}$ (kg $\cdot$ m^2) is the agent moment of inertia, $\phi_i(t)$ (rad) is the instantaneous orientation angle, $T_i^g(t)$ (N $\cdot$ m) is the instantaneous torque acting on the agent and dots indicate differentiation with respect to time. The movement of each agent in vertical direction, when relevant (e.g. on stairs – see Section A.9), is governed by geometrical constraints.

Each agent has its own characteristics (see A.2), and the global instantaneous force $\mathbf{F}_i^g(t)$ and torque $T_i^g(t)$ are given by the sum of different contributions. The various contributions model specific human behaviours or attitudes, namely: motive force/torque (see Section A.3), agent-agent interaction (see Section A.4), agent-wall interaction (see Section A.5), counter-flow (see Section A.6), and random force/torque (see Section A.7). Memory effects can also be introduced through so-called nervousness effects (see Section A.8). Furthermore, modelling is also needed to address agent-agent and agent-wall contacts/collisions (see Section A.11)

The Appendix describes in detail all aspects of the modelling, as well as the modifications introduced in the present model compared to the considered reference models. The developed modifications are diversified and range from small improvements and adaptations, or specific choices of parameters, to completely new modelling, depending on the case.

3. Development environment

While the presented model is suitable for classical batch simulations, the final target of the associated research, for which this paper represents the model development phase, is to explore the possibilities of human participation inside a simulation through the use of virtual reality (see [47]). As a result, the development environment was consequently chosen, making reference to the technology already available for games development. The simulation model was implemented through the game engine Unity3D [67], since it allows a direct implementation of real-time user interaction. Moreover, it also comes with tools that can be used effectively in the development process. The principal benefits from the selected development environment can be summarised as follows:

- The integration of the rigid-body equations of motions as well as the addressing of contacts can leverage on the integrated physics engine PhysX [52]. Moreover the physics engine offers an optimized ray-casting algorithm that has been used to prevent agents from interacting when separated by walls, decks, landings, stairs etc.
- The environment allows a direct importing and straightforward rendering of geometries described by generic 3D meshes.
- Within the development environment, the on-going simulation can be visualized in real-time, with the possibility to visualize and modify the simulation parameters on the fly.
- There is the possibility of easily implementing an interactive third person view of the simulation process allowing a real-time view of the on-going simulation. The view is based on clipping planes which is a feature very useful in case of ships where, typically, there are multiple decks.
- The deployed application can be run in batch-mode. Batch mode can be much faster than real-time, with the increase of speed depending on hardware, complexity of geometry and number of agents. This feature is relevant for classic design purposes, without human participation.
- The chosen environment features many tools to develop interactive virtual reality environments. It offers the possibility to add sound effects and lights to the scene. Moreover, it offers an implementation of a first person camera view that can be easily attached to an agent. Using this feature, a real-time human participation has been implemented [47–49], where users can control the motive force of an avatar while the other computer-controlled agents interact with the avatar as they would normally do with a standard agent.

During the development, some limitations associated with the choice of using a game engine environment have also been encountered, which can be summarised as follows:

- The physics engine uses single precision arithmetic to enhance performance. Due to single precision even deterministic simulations loose determinism when run on different platforms. Although results are qualitatively the same, cross-platform determinism is not guaranteed. However, simulation outputs are inherently stochastic (due to the aleatory uncertainty of the problem) and simulation results must be analysed in the ensemble domain. For this reason, even if two platforms provide different results for the same simulation input (for a fixed random seed value associated to the generation of random effects), the outputs deriving from Monte Carlo simulations and analysed in the ensemble domain are statistically equivalent.
- The collision model implemented in PhysX is not really suited for treating very high density situations, where many collisions occur at the same time and agents are almost constantly in contact with each other. The force-based spring-damper approach used by Helbing et al. [21] could be more suitable for these situations, but it requires significantly decreasing the integration time step, becoming problematic when the target is real-time simulations, as in the present case. Such situations are also difficult to be reproduced through virtual reality, due to the lack of perception of contact [57]. However, the contact model in the chosen development environment was considered to be appropriate for the purpose of the study reported herein, which addresses simulated and experimental conditions characterised by sufficiently calm egress where contacts are occasional and not continuous. Moreover, such an orderly evacuation condition is also the typical situation addressed from a design perspective.

The highlighted limitations, although worth to be borne in mind, have however not prevented an effective and fully functional implementation of the model within the Unity3D [67] environment.

4. Application

A series of test applications are reported in this section. These applications comprise two IMO test cases from MSC.1/Circ.1533 [32] where the developed tool is compared with results from FDS version 6.3.2 and Evac version 2.5.1 [40]. Subsequently, simulations are compared with experimental data regarding flow-density relations using a set of experiments provided by Zhang [76] and Zhang et al. [78]. Finally, a two-cabin-deck test case is presented as an extension of IMO Test 10. For the definition of the geometry of this latter example, reference was made to SAFEGUARD Validation Data Set SGVDS2 [1,5,10,62]. Results from the tool developed according to the presented model are hereinafter indicated as “UNITS”.

4.1. IMO test cases

MSC.1/Circ.1533 [32] suggests a series of test cases for the verification and validation of evacuation simulation tools. Herein, two test cases are considered, namely Test 8 and Test 11, whose outcomes are presented together with comparisons with results from FDS+Evac [40]. As described more thoroughly in the following subsections, IMO Test 8 addresses a situation of evacuation in the presence of counter-flow, while IMO Test 11 addresses a condition of evacuation through stairs. Both the tool developed herein as well as FDS+Evac fulfil the, mostly qualitative, requirements from MSC.1/Circ.1533 [32]. It is anticipated that the two test cases are passed by both tools. However, the comparisons highlight differences between the outcomes from the two tools, which stress the need for further comparisons possibly based on more quantitative experimental data. The main parameters used for IMO test case 8 and 11 are reported in Table 2.

4.1.1. IMO test case 8 – counter-flow condition

During the evacuation process there may be situations where agents are directed towards opposite or different directions. In the maritime field this may happen especially when the crew need to move towards internal zones of the ship while passengers need to move towards assembly stations. The flow rate in these counter-flow conditions is affected by the way people interact to avoid each other while moving towards the respective target. The IMO test 8 qualitatively addresses a counter-flow condition in terms of egress time, in order to assess the capability of the software to consistently model such a situation. The geometry of the test case is reported in Fig. 1.

Table 2
Main parameters used for IMO test case 8 and IMO test case 11 in MSC.1/Circ.1533 [32]

Agent radii	FDS+Evac "Male" class (see Table A.2)
Unimpeded speed v^U	Distribution U (0.97 m/s, 1.62 m/s)
Ascending stairs speed $v^{U\text{up}}$	$v^U \cdot 0.49$
Descending stairs speed $v^{U\text{down}}$	$v^U \cdot 0.66$

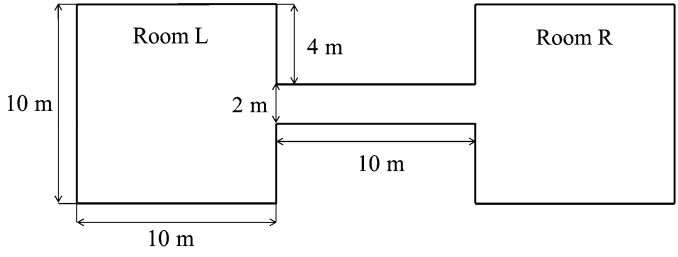

Fig. 1. Geometry of IMO test case 8.

The test comprises four different conditions. In the first one, 100 agents (group L) are placed at the back of the left room (room L) with an initial density of 3 p/m^2 and they are moving towards the opposite room, while the right room is empty. In the other conditions the number of people in the right room (group R), which are directed towards room L, is increased to 10, 50 and, finally, to 100. MSC.1/Circ.1533 [32] requires that the time the last agent in group L enters room R increases with the number of people starting from room R.

Results from simulations regarding agents initially in room L are shown in Fig. 2. A total of 250 independent realizations were carried out for each condition. The graphs show the time histories of 5%, 25%, 50%, 75%, 95% percentiles of the number of agents coming from room L and not yet in room R, as obtained from ensemble domain analysis at each time instant. It can be noticed that both models pass the test, as it is observed that the egress duration increases with the number of counter-flow agents.

In general, results from UNITS code show a faster exit (here exit is meant as the arrival in room R from room L) compared to FDS+Evac. Looking at the curves of instantaneous ensemble percentile levels, it can be noticed that the 95% one is the farthest from the others, indicating a long tail of the instantaneous distribution for the number of agents. This means that, in some cases, the exit time can be significantly larger than the median exit time, and this indicates the importance of reporting, in a detailed way, the aleatory uncertainty associated with the results of an evacuation analysis. It can also be noticed that the exit time from FDS+Evac increases much more significantly that in case of UNITS as the number of agents in counter-flow increases. From observation of the obtained simulations it could be noticed that this difference is due to the fact that in UNITS simulations the implemented counter-flow model tends to lead to the fast formation of two ordered lanes, which prevents the occurrence of jamming. Instead, the lane formation process in FDS+Evac simulations is slower and less organized, with a consequent increase of exit time. Using the median results as reference, the ratio between exit times from UNITS simulations and FDS+Evac simulations reduces as the number of counter-flow agents increases, giving ratios 0.94, 0.78, 0.68 and 0.62 for 0, 10, 50 and 100 counter-flow agents, respectively.

In order to analyse the differences in the formation of the lanes between the two models, the graph clustering method described by Schaeffer [65] has been used, which has already been used in the past also by Roggen et al. [61] to recognise group behaviour in crowds. The application of this approach (see [47]) showed that FDS+Evac simulations are characterised by a more noticeable presence of separate groups compared to outcomes from UNITS code, where agents tends to organise more orderly in lanes. FDS+Evac agents are therefore less organized than UNITS agents and the flow rate in FDS+Evac is often interrupted. The observed better organization behaviour arising in UNITS simulations is essentially due to the

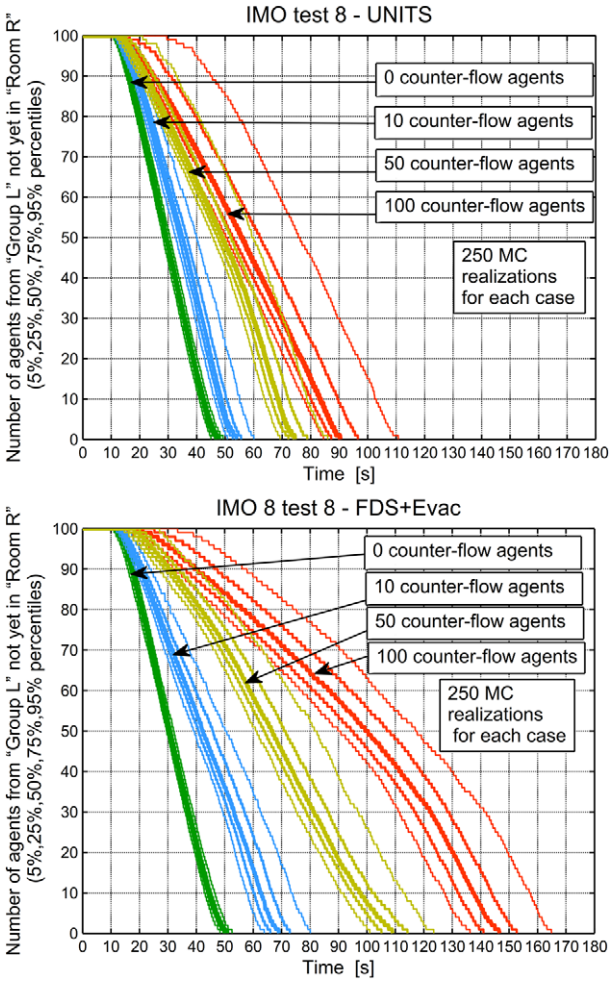

Fig. 2. IMO test case 8. Number of agents of group L not yet in room R (top: UNITS; bottom: FDS+Evac). Curves report 5%, 25%, 50% (median – thicker line), 75% and 95% percentiles from ensemble domain analysis of 250 realizations.

strength of the counter-flow force and to the parameter regulating the preferred direction.

The difference between UNITS and FDS+Evac results highlights the possibility of marked differences between two simulation models which are both passing the IMO test case 8, but it is not possible to decide on which model is more realistic in absence of experimental data. However, it is reasonable to suppose that experimental data could as well be influenced by variability of organizational skills depending on the tested population, similarly to what was observed by Chattaraj et al. [2] in

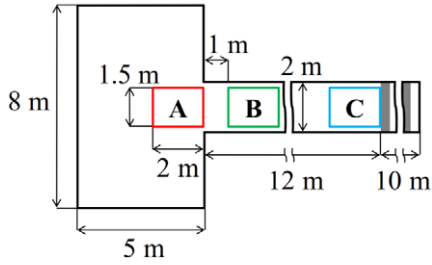

Fig. 3. Geometry of IMO test case 11.

case of tests related to flow-density relation analysis. The reported observations also highlight the value of assessing evacuation performance with different simulation tools.

4.1.2. IMO test case 11 – evacuation through stairs

The presence of stairs is inevitable in the vast majority of passenger ships. Moreover, elevators cannot be used during emergency conditions such as fire or flooding. During evacuations, congestions tend to be generated in front of stairs, due to the reduction in clear width and reduced velocity of evacuees on stairs. It is therefore important that software tools can accurately simulate the behaviour of passengers in such conditions. IMO test case 11 aims at testing the software's capability of correctly simulating congestion conditions at the entrance of stairs. The planar geometry of IMO test case 11 is shown in Fig. 3. Although the IMO test case 11 does not specify the characteristics of the stairs, herein a nominal stairway is considered with length of 10 m and height of 6 m, corresponding to an incline of 31°. In the test case, 150 agents are initially placed inside the room and are directed towards an exit, which is assumed to be placed at the end of the stairway. It is expected that congestion appears at the entrance of the corridor and at the beginning of the stairs, while a steady flow should originate within the corridor. In order to analyse the occurrence of congestion, time histories of agents' densities are calculated in areas A, B and C, indicated in Fig. 3.

Given a closed region Ω with area A_Ω (m^2) the instantaneous density $\delta_\Omega(t)$ (p/m^2) in the region Ω is determined as:

$$\delta_\Omega(t) = \frac{n_\Omega(t)}{A_\Omega} \tag{2}$$

where $n_\Omega(t)$ (p) is the number of agents inside the region Ω at time t. The density $\delta_\Omega(t)$ has been analysed from UNITS and FDS+Evac simulations on the basis of 250 random realizations for each simulation tool, and results are reported in Fig. 4.

Results in Fig. 4 indicate that, after the time necessary for the agents to reach the base of the stairs, the congestion is located only at the stairway entrance and the density in the corridor is low. As the simulation proceeds, the congestion spreads

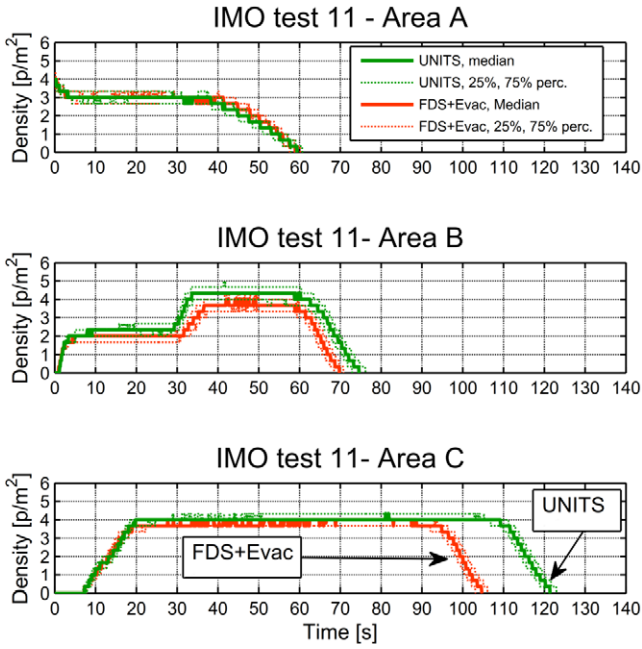

Fig. 4. IMO test case 11. Time dependence of density for different areas. Reported curves correspond to 25% (dotted lines), 50% (median – thicker lines) and 75% (dotted lines) percentiles from ensemble domain analysis of 250 different realizations.

upstream along the corridor reaching region B causing a sharp rise of density (approximately after $t = 30$ s). Afterwards, the density remains almost constant, until it decreases due to the fact that the room is progressively emptied. It can be noticed that the behaviour simulated by FDS+Evac and by the UNITS code is very similar, although FDS+Evac densities tend to be smaller. Furthermore, the total egress time from FDS+Evac is, for this test, shorter than that from the UNITS code.

Further insight into the time-space evolution of the density in the corridor can be obtained by analysing results from UNITS simulations, as reported in Fig. 5. The figure shows the average density, over 250 realizations, in rectangular regions placed at different positions along the corridor. The region of analysis is 1.5 m wide and 2 m long, as those in Fig. 3. The position of the measuring region is indicated by the coordinate x of its left edge, with $x = 0$ m corresponding to a region at the start of the corridor. The analysis is carried out with regions shifted by a spacing $\Delta x = 0.1$ m, covering the entire corridor.

Results in Fig. 5 clearly show the spreading of the high-density region from the bottom of the stairs upstream throughout the corridor. The spreading speed, corresponding to the slope of region characterised by the sharp density rise, is approximately 1.5 m/s. Within the high density region, some oscillations of density in time

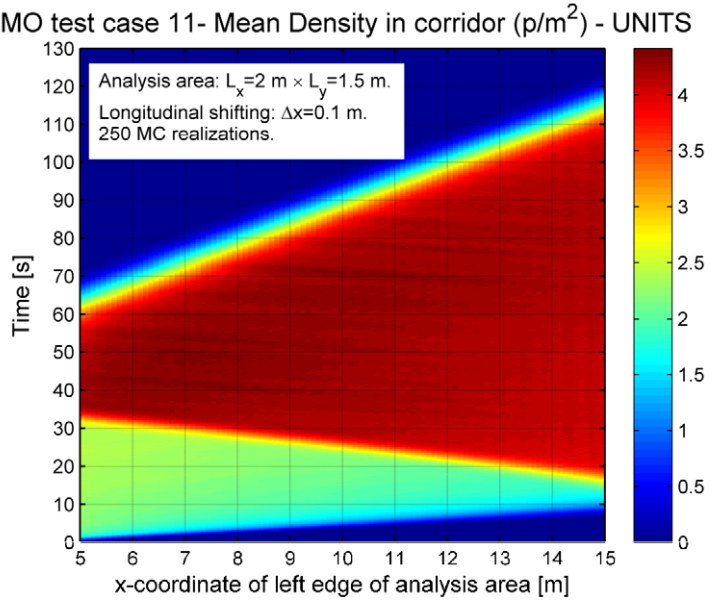

Fig. 5. IMO test case 11: time-space analysis of average density in the corridor (250 realizations). UNITS results.

and space are present. Subsequent observations of the simulation outcomes have shown that these oscillations are associated with the occurrence of stop-and-go phenomena, as described by Helbing et al. [22].

4.2. Flow-density relation

Relations between flow and density, or speed and density, play an important role in the estimation of evacuation performance of a designed ship arrangement. Qualitative requirements for the flow-density relations are present in MSC.1/Circ.1533 [32]. This relation was exhaustively discussed by Weidmann [73] who proposed an analytical relation between density and specific flow, i.e. the so-called "fundamental diagram". Subsequent investigations, e.g. Chattaraj et al. [2] and Zhang [76], have shown that such relations may depend on the specific geometrical details of the considered layout, or on pedestrian characteristics. In addition, it is worth noting that the concept of "fundamental diagram" is relevant also to the field of vehicular traffic analysis (e.g. [3,13,54]), where the focus is on speed/flow/density relations for vehicles rather than pedestrians.

The feature common to all fundamental diagrams is the fact that the specific flow (the flow normalized by facility width) grows with density until a certain value called "capacity of facility", and then it decreases, until it reaches zero (corresponding to the condition of jamming). This behaviour is mentioned in MSC.1/Circ.1533 [32],

where, in IMO test case 12, it is qualitatively required that the flow of persons in an unobstructed corridor is generally smaller at high densities compared with that obtained in case of low densities.

Due to the discrete Lagrangian nature of the agent-based microscopic model, the flow associated with a simulation run can be defined in different ways [76]. Considering the situation of a unidirectional flow in a rectangular corridor, the definition adopted herein for the instantaneous flow $\Phi_\Omega(t)$ (p/s), associated with the rectangular measurement region Ω having the same width of the corridor, is described by the following equation:

$$\Phi_\Omega(t) = \delta_\Omega(t) \cdot \bar{v}_\Omega \cdot b_{\mathrm{CORR}} \tag{3}$$

where $\delta_\Omega(t)$ is the density (p/m^2) as defined in (2), $\bar{v}_\Omega(t)$ (m/s) is the mean speed component of agents along the corridor axis within Ω, and b_{CORR} (m) is the width of the corridor.

Two cases are considered herein, for which experimental data are available, namely:

- A corridor [76];
- A T-junction ([76] and see also [78]).

Simulations are compared with available experimental data in the two mentioned cases in order to assess whether the expected qualitative behaviour for the flow-density relation is reproduced, and to analyse, for validation purposes, the level of agreement between simulations and experiments. According to Zhang [76], in both experimental test cases the population was composed of young adults having free walking speeds uniformly distributed in the interval 1.55 ± 0.18 m/s. Herein, such speed has been taken as the unimpeded walking speed of agents. In both cases the dimensions of agents in the simulations are taken in accordance with Table A.2.

Simulations have been carried out and analysed in accordance with the experiments and corresponding data analysis from Zhang et al. [77,78]. The flow-density relation was estimated by determining the density and the correspondent flow only in the portion of the simulations where the flow could be considered sufficiently stationary, neglecting, therefore, transients. A total of 100 realizations were carried out for each test case and time windows of stationarity were manually determined for each test case by analysing the time histories of ensemble mean values of density and speed.

4.2.1. Flow-density relation in a corridor

The case of evacuation through a corridor is relevant to the case of ship evacuation, as ship arrangements always feature corridors that may eventually be used during an evacuation process. Moreover, as one of the main targets of ship evacuation analysis is the detection of congestions (high density situations with low flow rate), the capability of an evacuation simulator to reproduce such congestions is clearly fundamental. Figure 6 shows the geometry of the test case by Zhang [76] characterised

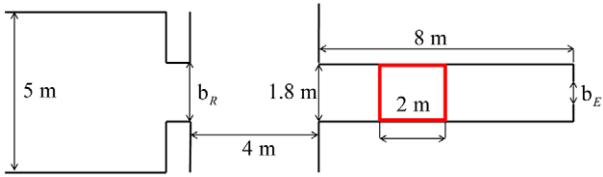

Fig. 6. Geometry of unidirectional flow experiment by Zhang [76].

Table 3
Parameters of considered corridor experiments, according to Zhang [76]

b_R(m)	0.50	0.60	0.70	1.00	1.80	1.80	1.80	1.80
b_E(m)	1.80	1.80	1.80	1.80	1.80	1.20	0.95	0.70
n	61	66	111	175	220	170	159	148

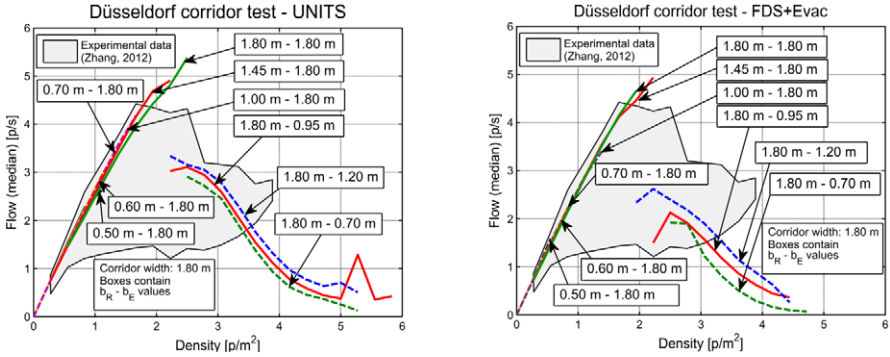

Fig. 7. Unidirectional flow test case. Flow-density relation. Left: UNITS results, Right: FDS+Evac results.

by a corridor width of 1.8 m. In order to change the density in the corridor, nine test conditions were considered by varying the room exit width b_R, the corridor exit width b_E and the number n of people, as reported in Table 3.

The flow–density relation as obtained by the UNITS code and by FDS+Evac are reported in Fig. 7. In order to compare simulations with the experimental results presented by Zhang [76], data are reported in terms of actual flow (see (3)) instead of the more commonly used specific flow (i.e. flow normalised by the width of facility). To avoid an excessive number of curves, the figures report only median values conditional to the density, as derived from the flow–density data obtained from simulations. Since experimental data have been reported by Zhang [76] in terms of scatter plots, herein reference experimental data are reported as areas where scatter data from Zhang [76] are (approximately) present.

Results in Fig. 7 show that the main patterns of the flow-density relation are reproduced by the simulations. The maximum flow corresponds to a density of ap-

proximately 2 p/m^2, which is in agreement with test results and with most of the fundamental diagrams presented by Chattaraj et al. [2]. There is a notable difference between the simulated flow rate of those situations where the exit has the same width as the corridor ($b_E = 1.8$ m) and those where the exit is narrower than the corridor ($b_E < 1.8$ m). These two conditions are also linked with the marked discontinuity, located approximately at density of 2 p/m^2, which can be clearly noticed in both UNITS and FDS+Evac results. The observed differences can be associated to the fact that when the exit width is narrower than the corridor width, agents have to organize to exit from the corridor, and this generates situations with high density but very low speed in both UNITS and FDS+Evac simulations. Instead, according to the scatter plots by Zhang [76], the actual behaviour from experiments seems to be smoother. Moreover, experiments do not reach densities as high as those reached in the simulations. This might be due to the fact that humans can organize better than simulated agents when exiting from the bottleneck. It is also reasonable to think that people try to slow down in advance if they see a clogging ahead, and this behaviour might prevent the density from rising to high values. Instead, in the social force models characterised by short-range interaction forces, agents slow down only when they are very close to other agents, and this results in higher density conditions.

UNITS results in Fig. 7 show also a peculiar behaviour in the region of very high density, around 5 p/m^2. Specifically, for $b_R = 1.80\text{ m} - b_E = 0.95$ m there is a marked local peak in the value of flow, and a similar, but smaller peak is visible also for the case with $b_R = 1.80\text{ m} - b_E = 1.20$ m. A direct comparison with FDS+Evac is not possible, because simulations from FDS+Evac do not reach such high densities. The exact reason for the appearance of this behaviour in UNITS simulations is not clear at this stage, but it may be the result of specific combinations of parameters (force modelling, exit width, dimensions of agents, etc.) that favour a faster flow. It shall also be noted that the available data sample in the region of high densities is more limited, and this leads to higher sampling uncertainty in the analysis of data. Overall, this is an observed result that would be worth additional investigation.

The analysis of aleatory uncertainty associated with simulated data offers valuable additional information also in this situation. Figure 8 presents scatter plots from simulations using the tool developed herein, together with 5%, 25%, 50%, 75%, 95% percentiles (conditional to density). The observed spread of data indicates the difficulty in the quantitative determination of a representative flow-density relation with too few tests. The dispersion of flow data conditional to the density is smaller in low-density conditions and larger in high-density conditions. An increase of conditional dispersion of flow given density in high-density conditions can also be noticed in the experimental scatter plots from Zhang [76]. This behaviour shows that, while for relatively low densities the flow-density relation is well determined by the unimpeded speed and by the geometry, in high density conditions the capability of organization of people has an important effect and can lead a high level of uncertainty.

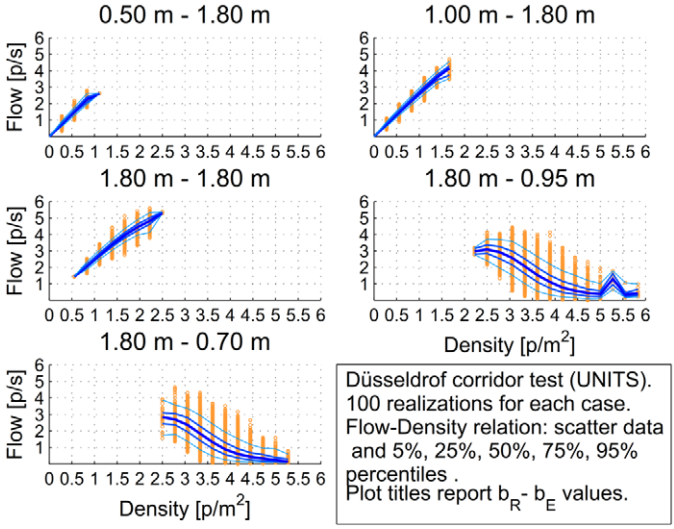

Fig. 8. Unidirectional flow test case. Scatter plots and 5%, 25%, 50%, 75%, 95%, conditional percentiles of flow given density for a set of different simulation conditions.

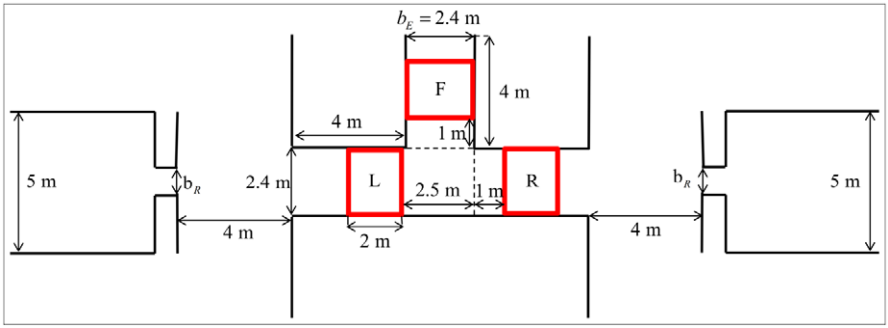

Fig. 9. Geometry of the T-junction test case. Reference areas are highlighted: left region (L), right region (R), front region (F).

4.2.2. Flow-density relation in a T-junction

T-junctions are a type of element which is typically present in the arrangement of vessels [32,62], especially in case of large passenger vessels with cabin areas. The flow-density relation inside a T-junction can be different from the one measured in a simple corridor, as observed by Zhang [76] and Zhang et al. [78]. Moreover, the flow-density relation is also different depending on the specific measurement area in the T-junction. A comparison between data provided by Zhang [76] and Zhang et al. [78] and simulation results obtained from FDS+Evac and the UNITS code was therefore performed. Figure 9 shows the geometry of the T-junction used in

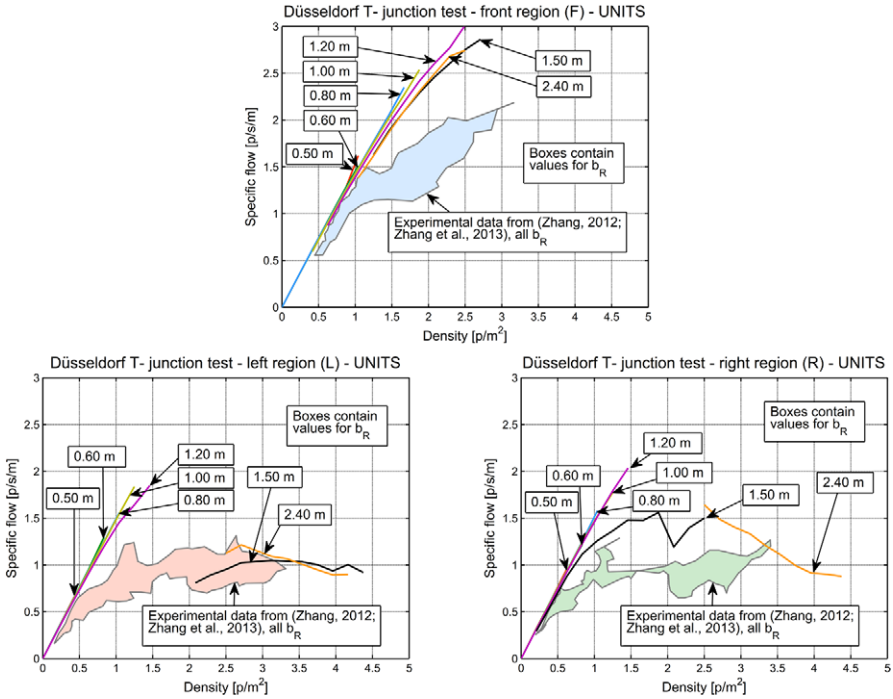

Fig. 10. T-junction test case. Conditional median specific flow for each test condition and for each measurement area (top: front region-F; bottom left: left region-L; bottom right: right region-R), as obtained from the analysis of UNITS simulations, and comparison with experimental data. Boxes contain the value of the exit width b_R. Total number of realizations in the Monte Carlo simulations: 100.

the experiments by Zhang [76] and Zhang et al. [78]. The properties of the agents population used for the simulation are the same as the ones specified in Section 4.2.1 herein, for the corridor test case.

In order to allow comparison with experimental data presented by Zhang [76] and Zhang et al. [78], results are reported in this section in terms of specific flow (flow normalized by the width of facility). Figure 10 reports UNITS results as conditional median specific flow for each test condition and for each region highlighted in Fig. 9. A total of 100 Monte Carlo realizations were carried out, and, in the analysis of simulations, only data at stationary states were considered. The figure also reports an indication of the region of graph corresponding to the experimental scatter data from Zhang [76] and Zhang et al. [78] for all values of b_R.

From results in Fig. 10, a series of considerations can be done. For both the left and right region, simulated cases with $b_R = 1.50$ m and $b_R = 2.40$ m allow reaching higher densities compared to the other configurations ($b_R = 0.50$ m, 0.60 m, 0.80 m, 1.00 m, 1.20 m). However, the flow-density relation obtained by simulations seems to be smoother for the right region compared to the left region. In fact, in the left

region there seems to be a sharp decrease, or a discontinuity, or a gap, in the region of densities around $1.5 \div 2.0$ p/m^2. Instead, in case of the right region, there seems to be a smoother transition between the low-density and the high-density conditions. However, experimental data show a more similar and smooth behaviour for the right and left regions. In the front region, conditions of very high densities are not reached, neither in the simulations nor in the experiments. Nevertheless, the specific flow appear to keep on increasing for a wider range of densities compared to the left and right regions, both in the experiments and in the simulations. Although simulation results do not match quantitatively well the experimental data, it looks like the trend is nevertheless qualitatively captured. Also for the present case of T-junction an analysis of scatter data was carried out, which, similarly to the case of unidirectional flow (see Fig. 8), highlighted a larger dispersion in case of high density compared to the case of low density.

Finally, Fig. 11 compares simulation results from both UNITS code and FDS+Evac with experimental data by Zhang [76] and Zhang et al. [78], by joining data from all conditions with different exit widths b_R. Outcomes from FDS+Evac and UNITS show flow rates which are in general higher than those obtained from the experiments, especially in intermediate-density conditions. However, it is to be noted

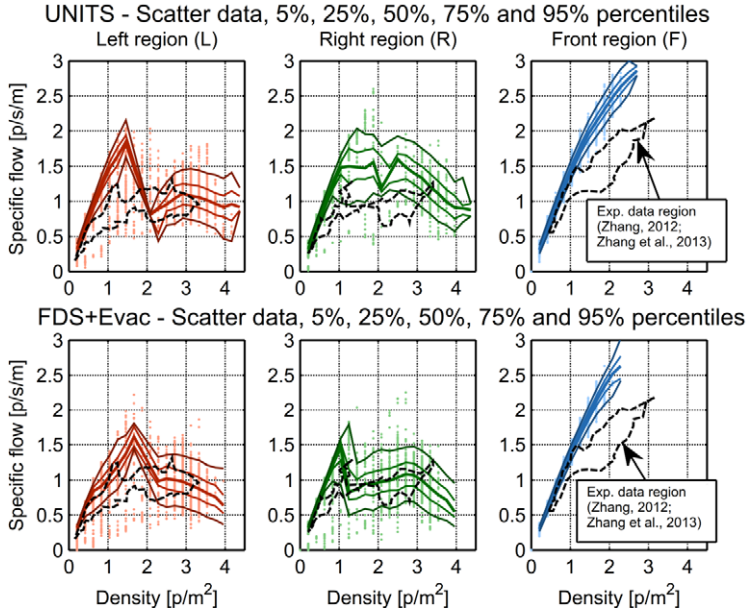

Fig. 11. T-junction test case. Comparison between experimental data from (Zhang [76]; Zhang et al. [78]) and simulations for all values of exit width b_R. Top: UNITS, bottom: FDS+Evac. Graphs report scatter data and conditional specific flow percentiles (5%, 25%, 50%, 75% and 95%), together with the region associated with experimental data. Total number of Monte Carlo realizations in the simulations: 100 for each value of exit width b_R.

that experimental values reported by Zhang [76] and Zhang et al. [78] show that the speed of the subjects during the tests was lower than the average unimpeded speed, even in condition of very low density. This means that there was a tendency from the subjects, during the tests, to move slower than in unimpeded conditions even in situations without obstacles. This might be explained by the fact that people in a T-junction, knowing that they will eventually have to change direction, tend to slow down with respect to a corridor situation, and this type of behaviour is not modelled in the two simulation codes which are characterised by relatively short-range interactions among agents.

A qualitative difference in the specific flow-density diagram between the front and lateral (right and left) areas can be observed both from FDS+Evac and UNITS simulations. A qualitatively similar difference is present also in the experimental data, as visible in Fig. 11 and as remarked also by Zhang [76] and Zhang et al. [78]. In the front area the specific flow-density diagram shows an almost linear behaviour both in case of FDS+Evac and UNITS, with a limited saturation at higher densities. Instead, experiments from Zhang [76] and Zhang et al. [78] show, first, an almost linear increase of specific flow with density (up to about 1 p/m^2), and then a reduced increasing trend with an increase in the data dispersion. This particular characteristic from experimental data might be due to the fact that, in the real situation, people tend to change their desired speed when they see many other people coming from the opposite direction, and this type of behaviour is not modelled in the two simulation codes which, as said before, are characterised by relatively short-range interactions among agents.

In the lateral (right and left) areas, the increase of specific flow with the density tends to saturate early, and simulations overpredict the initial growth of specific flow for low densities. FDS+Evac and UNITS codes show similar outcomes in the left region, whereas they differ more markedly in the right region. In the left region, both UNITS and FDS+Evac show a sharp decrease, almost a jump, of specific-flow when the density exceeds approximately 1.5–2.5 p/m^2, although such jump is more evident in case of UNITS. In the right region, a jump is visible in FDS+Evac outcomes above a density of about 1 p/m^2. Below this density, experimental data are overpredicted, while FDS+Evac shows a better matching with experiments at higher densities. Instead, results from UNITS in the right region do not show such a jump, and the specific flow, after a first increase, remains almost invariant for densities in the range 1.0–2.5 p/m^2, and then it slowly decreases. In general, UNITS simulations in the right region tend to overpredict the specific flow in comparison to the experimental data. This discrepancy between simulations from UNITS and experimental data might be due to the combination of two factors. Firstly, the unimpeded speed suggested by the experimental measurements could be too high for use in the considered T-junction condition, and this is indicated, in particular, by the results in the front region. Secondly, another source of discrepancy could be a too strong right preference in the counter-flow model.

4.3. Two-cabin-deck test case

In this section, a test geometry is proposed which is directly relevant to the maritime field. Scope of the proposed geometry is to be complex enough for being representative of a realistic case, while still being sufficiently simple to allow comparative exercises and code testing without too significant efforts in the geometrical modelling of the environment. The arrangement of the proposed geometry is presented in Fig. 12. The proposed geometry was derived as a direct simplification of the geometry from the SAFEGUARD Validation Data Set 2 (SGVDS2) [11], which corresponds to the case a cruise vessel. For the development of the simplified geometry in Fig. 12, the aft portions of decks 5, 6, 7 of the entire SGVDS2 were considered. Decks 5, 6, 7 from SGVDS2 correspond to decks 1, 2, 3 in Fig. 12. Deck 2 and deck 3 are cabin decks having the same layout, while an assembly station is assumed to be placed on deck 1, as a simplification of the corresponding one on deck 5 of SGVDS2. The connection between the decks is made through a single staircase that

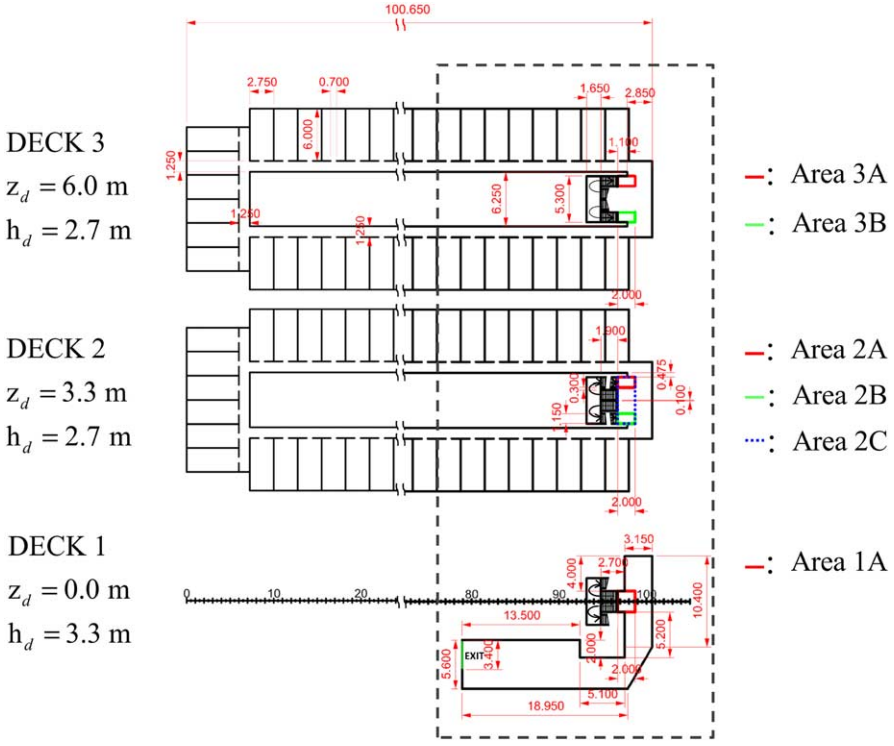

Fig. 12. Arrangement of the two-cabin-deck test case. The variable z_d indicates the vertical coordinate of each deck plane, while h_d indicates the height of each deck. Areas used for the analysis of simulations are indicated as 1A, 2A, 2B, 2C, 3A and 3B.

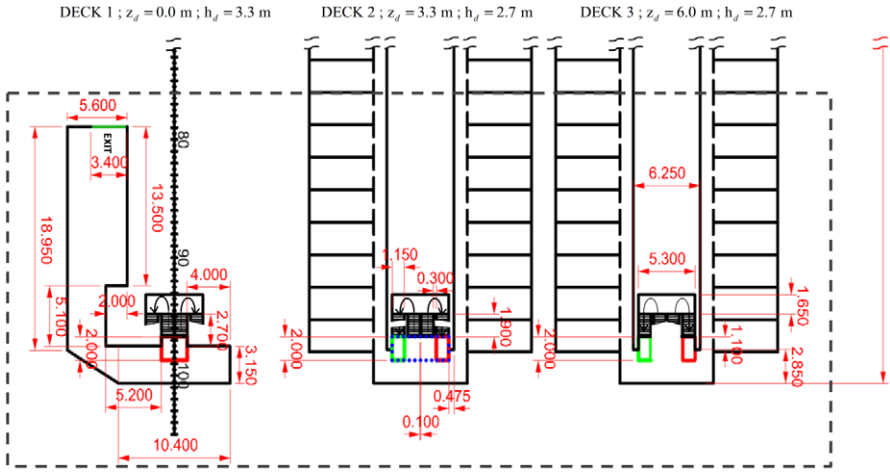

Fig. 13. Arrangement of the two-cabin-deck test case. Detailed view close to the staircase.

rises from deck 1 to deck 3, and this staircase corresponds to stairs 8, 10 and 12 from the SGVDS2 geometry. For the sake of simplification, all cabins in Fig. 12 have the same dimensions and the exit of each cabin is placed in the middle of the corresponding side. The dimensions of stairs and landings, as well as the heights of the decks are the same as those reported by Galea et al. [11]. All landings are positioned at mid-height between the corresponding upper and lower decks. Figure 12 provides detailed measurements as well as the indication of areas which are used for the analysis of simulations. An enlarged view of the portions of deck close to the stairs is shown in Fig. 13.

An evacuation scenario has then been setup. In order to observe clogging phenomena and clearly identify conditions of high density, two agents are placed within each cabin at the starting of the simulation, for a total of 288 agents. Agents distribution follows the age/gender population groups distribution reported in Table 3.1 in MSC.1/Circ.1533 [32]. For each ith agent, the unimpeded speed on stairs was defined to be proportional to the unimpeded speed on flat terrain, v_i^u. The proportionality is reflected through two coefficients, namely $k^{S,\mathrm{up}}_{\mathrm{group}(i)}$ and $k^{S,\mathrm{down}}_{\mathrm{group}(i)}$, that depend on the group the ith agent belongs to (see Table 4). The coefficients of proportionality were set by noting that the bounds of the intervals of unimpeded speed on stairs in Table 3.5 of MSC.1/Circ.1533 [32] scale with an approximately constant coefficient with respect the bounds of the intervals of unimpeded speed on flat terrain in Table 3.4 of MSC.1/Circ.1533 [32]. Such coefficients of proportionality are reported in Table 4. Agent dimensions for males and females were distributed according to Table A.2. For the sake of simplification, the response time was set to zero for all agents. Therefore, all agents start moving at the same time, corresponding to the beginning of the simulation. The scenario was simulated through a total of 250 Monte Carlo realizations.

Table 4

Coefficients $k^{S,\text{up}}_{\text{group}(i)}$ and $k^{S,\text{down}}_{\text{group}(i)}$ for the determination of unimpeded speed on stairs. Based on analysis of data from IMO MSC.1/Circ.1533 [32] (Table 3.1, Table 3.4 and Table 3.5 therein)

	Population group – passengers									
	G1	**G2**	**G3**	**G4**	**G5**	**G6**	**G7**	**G8**	**G9**	**G10**
$k^{S,\text{up}}_{\text{group}(i)}$ [-]	0.51	0.62	0.65	0.65	0.63	0.45	0.49	0.45	0.46	0.45
$k^{S,\text{down}}_{\text{group}(i)}$ [-]	0.60	0.69	0.80	0.79	0.79	0.68	0.66	0.60	0.60	0.60

Unimpeded speed on stairs for ith agent: $v_i^{\text{u,up/down}} = k^{S,\text{up/down}}_{\text{group}(i)} \cdot v_i^{\text{u}}$.

G1: Females younger than 30 years; **G2:** Females 30–50 years old; **G3:** Females older than 50 years; **G4:** Females older than 50, mobility impaired (1); **G5:** Females older than 50, mobility impaired (2); **G6:** Males younger than 30 years; **G7:** Males 30–50 years old; **G8:** Males older than 50 years; **G9:** Males older than 50, mobility impaired (1); **G10:** Males older than 50, mobility impaired (2).

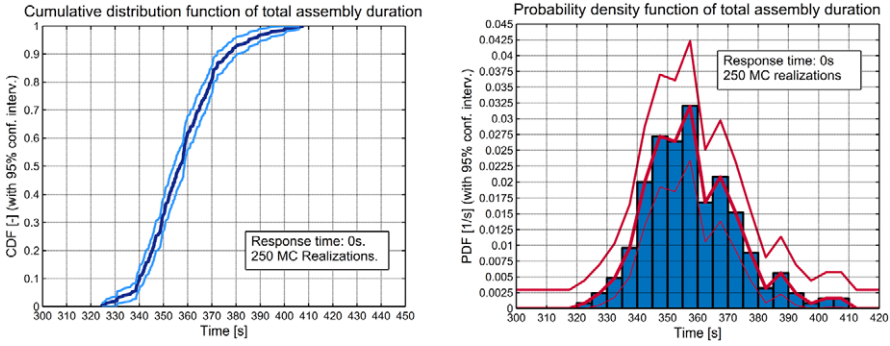

Fig. 14. Two-cabin-deck test case. Estimated cumulative distribution (CDF), left, and probability density function (PDF), right, of total assembly duration. Thick lines correspond to estimated values, while thin lines correspond to limits of 95% confidence intervals for the estimations. The graph of the estimated PDF reports data also in the form of bars, in order to show the width of the bins used for the estimation of the PDF.

First, Fig. 14 shows the cumulative distribution and the probability density function of the total assembly duration, which, in this case, corresponds to the time elapsed between the beginning of the simulation and the time instant the last agent arrives at the designated assembly station by exiting from the exit on deck 1.

The total assembly time from the simulations as analysed in Fig. 14 shows a significant dispersion when considering, particularly, extreme values. Data are characterised by a median of 357 s, 10% percentile of 340 s, 90% percentile of 377 s, observed minimum 325 s, observed maximum of 408 s, and most probable value approximately around 355 s.

Evacuation simulation tools are expected to be used also to detect points of high congestion in case of ship evacuation. When using advanced evacuation analysis tools, MSC.1/Circ.1533 [32] defines as congestion regions those regions having density higher than $4 p/\text{m}^2$ for a significant duration. The density from simulations in

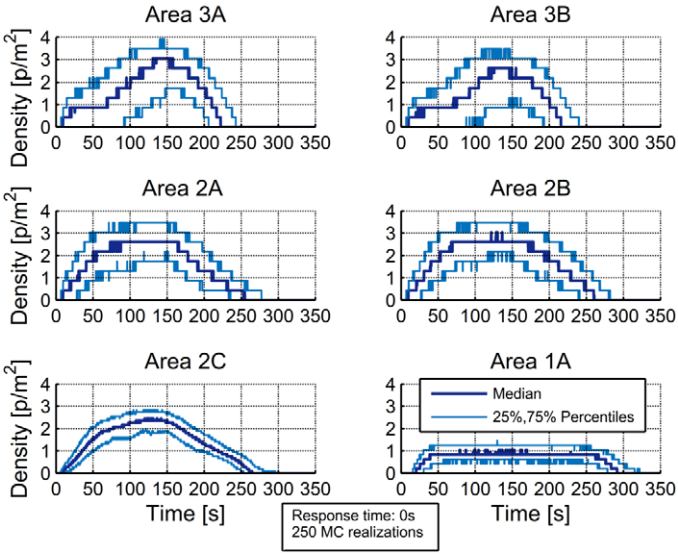

Fig. 15. Two-cabin-deck test case. Density inside each area in front of the stairs. The curves report the ensemble 5%, 50% and 95% percentiles for each time instant. Total number of Monte Carlo realizations: 250.

areas 1A, 2A, 2B, 2C, 3A and 3B (see Fig. 12) is analysed in Fig. 15, and it can be noticed that it rarely exceeds 3.5 p/m^2. As a result, following the definition from MSC.1/Circ.1533 [32], in the considered test scenario, there were no congestions in the considered regions. Nevertheless, situations of high density could be identified at the entrance of stairs. Such regions of high density are the most likely to become congestion regions in situations of panic and nervousness.

Looking at results in Fig. 15 it can be noticed that the density increases at the entrance of the staircases. The lowest densities are observed for the area 1A, because agents in that region are exiting from the stairway already organized in ordered lanes and no clogging occurs. The density in area 1A, after a first raising, then remains, on average, constant, until the evacuation has completed. On the other hand, all regions at the entrance of stairs (areas 2A, 3A, 2B, 3B) show an initial strong increase of density that then decreases as the decks and the staircase progressively get empty. While for areas 3A and 3B there are no long stationarity time windows, stationarity time windows can be identified for areas 2A and 2B in correspondence to the highest density. It is also worth noticing that, for areas 3A and 3B, the rise of density occurs in two phases. In a first phase the density increases slightly, while in a second phase the density increases faster towards the maximum value after which it sharply decreases. The density in the area 2C is lower than the ones measured in area 2A and area 2B, particularly in the time window where densities are increasing. This is due to the fact that area 2C comprises also the region in front of the stairs descending

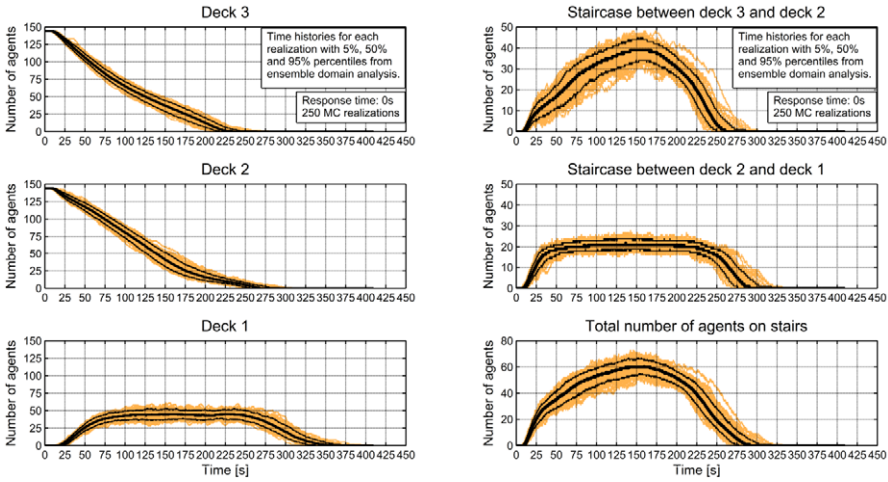

Fig. 16. Two-cabin-deck test case. Number of agents in each deck (left) and staircase (right). The figure reports time histories from each single realization, as well as 5%, 50% and 95% percentiles from ensemble domain analysis at each time instant.

from deck 3, where the density is low as descending agents are already organized in ordered lanes. The stationarity time windows with high density in areas 2A and 2B are longer than those in areas 3A and 3B. This might be due to the situation occurring at the entrance of the stairs leading from deck 2 to deck 1. In fact, in such region, agents descending from deck 3 and, arriving on deck 2, compete for the occupancy of the stairs with agents coming from the cabins on deck 2.

The overall flow of passengers can be better understood by considering the distribution of the number of people inside each deck and staircase, at each time instant, as reported in Fig. 16. From the results, it can be noticed that, while the flow is similar for agents in deck 2 and deck 3, there is a very marked difference between the staircase between deck 3 and deck 2 and the staircase between deck 2 and deck 1. The large number of agents inside the staircase between decks 3 and deck 2 is due to the fact that agents descending from deck 3 compete to access the staircase between deck 2 and deck 1 with agents coming from cabins in deck 2, as previously highlighted. This situation of competition for the use of the facility slows down the flow of agents inside the staircase between the deck 3 and deck 2 (occasionally blocking the flow) and causes a situation of high density inside the staircase. This observation is in agreement with the behaviour of the density as presented in Fig. 15. In general, this type of information, when reported for real ship arrangements, can be useful for better understanding the capacity of the facilities and for driving design choices, such as the selection of stairs width, aimed at optimizing the evacuation performance of the ship arrangement.

Finally, Fig. 17 summarises the flow of agents in the considered evacuation scenario, by reporting the distribution of number of exited agents at each time instant

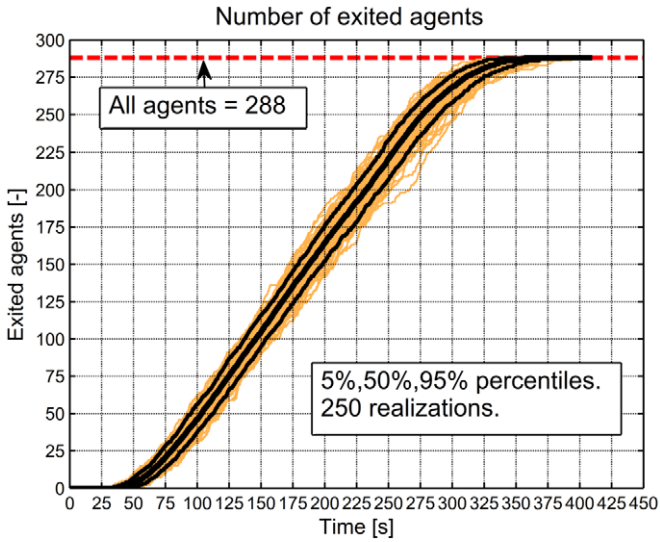

Fig. 17. Two-cabin-deck test case. Analysis of time dependence of number of exited agents. The figure reports time histories from each single realization, as well as 5%, 50% and 95% percentiles from ensemble domain analysis at each time instant.

from the ensemble domain analysis. It can be noticed that, despite the previously observed large variability of behaviour in different regions in different decks, the global exit rate is almost constant for a large portion of the simulation time.

5. Conclusions

This paper has presented the development of an agent-based modelling for evacuation simulation that can be used for performing advanced evacuation analyses as prescribed by the MSC.1/Circ.1533 [32]. As primary goal, the model has been developed for implementation in a software intended to also allow the possibility of real-time human participation during the evacuation simulation, in an immersive virtual reality environment. At the same time, the model is suitable also for standard evacuation simulations.

The mathematical model for the dynamics of agents is based on the social forces approach introduced by Helbing and Molnar [23]. More specifically, the FDS+Evac social force model, as described by Korhonen [40], was taken as main starting point. A series of modifications to the models by Helbing and Molnar [23] and Korhonen [40] have then been introduced, as improvements, modifications, new modelling, or adaptations for use in real-time immersive virtual reality simulations. There were several reasons for modifying the reference models. On the one hand, from a general perspective, development was carried out to address some criticalities identified

when using the original reference models, to try improving the robustness and simulation performance compared to the original models, and to try to achieve a better tuning of some modelling parameters. On the other hand, some modifications have been introduced to make the model better suited for applications targeting real-time human participation and to better adapt the model to the used development environment. The developed model has been described in detail. The described model has been implemented in a software tool through a game engine, and benefits and limitations of this choice have been described.

In order to perform a verification and validation process, the developed tool has been tested considering MSC.1/Circ.1533 [32] and experimental data from Zhang [76] and Zhang et al. [78]. In this process, comparisons have also been carried out with outcomes from FDS+Evac. Particular attention was given to the quantification and reporting of aleatory uncertainty.

With reference to IMO test cases, test 8 (counter-flow) and test 11 (staircase) were considered. In the IMO test case 8, the new counter-flow model developed herein showed a tendency to lead to a relatively quick and ordered organization of agents in lanes. Globally, this led to faster flow rates compared to FDS+Evac. In the IMO test case 11, the model developed herein led to slightly higher densities compared to FDS+Evac. An analysis of the time-space dependence of the density within the corridor was also carried out, showing the details of the propagation of the congestion.

The developed software has been compared, in parallel with FDS+Evac, with experimental data from Zhang [76] and Zhang et al. [78] regarding the flow-density relation (fundamental diagram) in a corridor and in a T-junction. Simulations could reproduce experimental data qualitatively, and, in some conditions, also quantitatively. Generally, the level of scattering (statistical dispersion) of experimental data was well reproduced. In case of the T-junction, outcomes from the simulations generally showed higher flow rates compared to the experiments. The analysis also showed the importance of reflecting the underlying aleatory uncertainty when reporting experimental and simulation results. The interpretation of the obtained results seems to indicate that the considered social force modelling, although providing reasonable results, would benefit from improvements in order to better reflect complex organization capabilities of people in evacuation conditions. In fact, the social force models used in this study are based on relatively simple short-range interactions among agents. These models do not reflect the fact that, during an evacuation, human behaviour may be affected also by the evacuees level of knowledge of the situation, concerning the space topology, the density conditions, etc. Evacuees may take into account both instantaneous conditions, as well as future estimated conditions. Those estimates may be based not only on a short-range type of assessment. They may also be performed in a long-range fashion and used to adjust the speed or choose the path to follow.

Finally, a more realistic test case, more specific to the maritime field, has been proposed. The geometry of the proposed test case was derived as a simplification of the SAFEGUARD Validation Data Set 2 [11], and it comprises three decks connected by

staircases, with the two uppermost decks being cabin decks. A simplified evacuation condition has been simulated with the developed software, considering all cabins occupied. Detailed results have been reported by also highlighting and quantifying the underlying aleatory uncertainty. All necessary information has been provided to allow a reproduction of the proposed two-cabin-deck test case, which could be used for comparisons among different mathematical models/tools.

Further developments of the tool, concerning the development of the interface for implementing real-time human participation, as well as testing of actual real-time human participation, have been provided by Montecchiari [47] and Montecchiari et al. [48,49]. Experiments with human interaction may open the way to calibration, and possibly validation, of evacuation models, not only through complex real experiments as presently done, but also through the use of virtual reality. Moreover, validated software allowing real-time human participation could also be used for training of the crew and of the passengers in simulated situations of danger. Finally, interactive simulations can also have applications in ship design by giving the designer the possibility of having a better perception of the evacuation process through a first person view or through the possibility of virtually, but actively, taking part to the evacuation.

It is noted that this paper has not addressed, in the mathematical model, the possible movement of the platform. According to present IMO guidelines, it is not required to include the effects of ship motions when carrying out the evacuation analysis. However, ship motions, when present, may influence the evacuation process, depending on their severity. Extension of the modelling to account for effects of ship motions has been investigated by Montecchiari [47].

Acknowledgements

The research activity of Gabriele Montecchiari has been carried out in the framework of his Ph.D. programme at University of Trieste (Ph.D. scholarship G/3-Cycle XXX financed by MIUR “Progetto Giovani Ricercatori” through University of Trieste).

Appendix. Detailed description of mathematical model

As anticipated in the main text, the simulation approach presented herein is based on the social force approach, and it has been developed starting from Helbing and Molnar [23] and the model embedded in FDS+Evac [40], implementing a series of modifications to such models.

In the developed model, agents move in a 2-dimensional manifold. Agents and obstacle are modelled in 2-dimensions (considering the projection on the XY-plane),

while the third component is treated separately and derives from geometric constraints.

Each agent is thus considered as a rigid body having three degrees of freedom: the translation along x-axis and y-axis, and the rotation around the vertical axis. The 2-dimensional movement (translation and rotation) of each agent is described by rigid body dynamics laws. For translation, the equation of motion is

$$m_i \cdot \ddot{\mathbf{x}}_i(t) = \mathbf{F}_i^g(t) \tag{A.1}$$

where m_i (kg) is the mass of the ith agent, $\mathbf{x}_i(t)$ (m) is its instantaneous position vector, $\mathbf{F}_i^g(t)$ (N) is the global instantaneous force vector acting on the ith agent, and dots indicate differentiation with respect to time. The rotation around the agent's vertical axis is described by the following equation:

$$I_{z,i} \cdot \ddot{\phi}_i(t) = T_i^g(t) \tag{A.2}$$

where $I_{z,i}$ (kg $\cdot$ m^2) is the agent moment of inertia, $\phi_i(t)$ (rad) is the instantaneous orientation angle, $T_i^g(t)$ (N $\cdot$ m) is the instantaneous torque acting on the agent.

The agent's translational movements are caused by the global force $\mathbf{F}_i^g(t)$, which is applied at each time step of the simulation and is the sum of different contributions, modelling specific human behaviours or attitudes. Table A.1 provides a summary of the different contributions to the global force and torque.

As social forces are all applied to the agents' centre of mass they do not generate torque. The change of body orientation is, instead, modelled separately through social torques. In this way social torques are complementary to social forces in modelling each specific behaviour/condition. A more detailed description of the modelled forces and torques is given in the relevant subsequent sections of this appendix.

As it can be noted from Table A.1, a random force and a random torque are also applied during the simulation, and their role is twofold. On the one hand, they mimic a certain level of inherent natural randomness in the agents' behaviour. On the other hand, the addition of a random noise prevents unnatural impasse situations (equilibria of the dynamical system) from occurring.

Table A.1

List of forces/torques and associated behaviours

Type of action/interaction	Symbol	Behaviour
Motive force and torque	$\mathbf{F}_i^{\text{mot}}$, T_i^{mot}	Agents are oriented and move towards their target.
Agent-agent interaction	$\mathbf{F}_i^a$, T_i^a	Agents avoid collisions with other agents.
Wall-agent interaction	$\mathbf{F}_i^w$, T_i^w	Agents avoid collisions with walls.
Counter-flow	$\mathbf{F}_i^{\text{cf}}$, T_i^{cf}	Agents modify direction and orientation if in counter-flow.
Random force and torque	$\mathbf{F}_i^{\text{rand}}$, T_i^{rand}	Random fluctuation.

Detailed description of the modelling is given in the subsequent sections of this appendix, but the main modifications that have been introduced in the presented modelling compared to the reference models [23,40] can be summarised as to have addressed the following aspects:

- Limitation of forces (see Section A.1);
- Motive force (see Section A.3);
- Counter-flow (see Section A.6);
- Model of random forces (see Section A.7);
- Modelling of nervousness effects (see Section A.8);
- Stairs model (see Section A.9);
- Effect of vertical direction in social forces (see Section A.9);
- Interaction with walls and obstacles (see, in particular, Sections A.5 and A.11);
- Route finding (see Section A.10).

The introduced modifications make the present modelling different from what is presently available in literature, while still remaining in the framework of the social force modelling.

It is further noted that the motion of the agents is governed by the mentioned 2-dimensional rigid body dynamics laws in open space, with the exception of contact situations. Usually, social force models use a spring-damper approach to model contacts [23,40,45]. Instead, in the presented model, contacts are managed directly by the physics engine embedded in the development environment (see Section A.11).

The following subsections provide a detailed description of the simulation model.

A.1. Clamping of global force and torque

In principle, the global force $\mathbf{F}_i^g$ acting on the agent is the sum of the different force contributions mentioned in Table A.1. However, while motive force values are typically associated with corresponding accelerations (forces per unit mass) close to real measured acceleration values, the models for the repulsive and counter-flow forces can lead to very high forces per unit mass. As a result, a direct summing of the single contributions can lead to unrealistic agents accelerations. This phenomenon was observed also by Lakoba et al. [42]. To address this situation, the raw global force, in the model presented herein, is subject to a two-step clamping procedure.

The two-step clamping procedure is based on the reported considerations. Since the sum of the forces $\mathbf{F}_i^{\mathrm{cf}}$, $\mathbf{F}_i^a$ and $\mathbf{F}_i^w$ can lead to large values of force per unit mass, this sum is subject to a first clamping stage. Subsequently, this, possibly clamped, sum of forces is added to the motive force $\mathbf{F}_i^{\mathrm{mot}}$ and to the random force $\mathbf{F}_i^{\mathrm{rand}}$. The force obtained by this second summation is subject to a second clamping stage, to avoid the possibility of too large accelerations. The described two-step clamping can

formulated as follows:

$$\begin{cases} \mathbf{F}_i^{p,*}(t) = \mathbf{F}_i^{\mathrm{cf}}(t) + \mathbf{F}_i^{a}(t) + \mathbf{F}_i^{w}(t) \\ \mathbf{F}_i^{p}(t) = \min(\|\mathbf{F}_i^{p,*}(t)\|, m_i \cdot b_f) \cdot \frac{\mathbf{F}_i^{p,*}(t)}{\|\mathbf{F}_i^{p,*}(t)\|} \\ \mathbf{F}_i^{g,*}(t) = \mathbf{F}_i^{p}(t) + \mathbf{F}_i^{\mathrm{rand}}(t) + \mathbf{F}_i^{\mathrm{mot}}(t) \\ \mathbf{F}_i^{g}(t) = \min(\|\mathbf{F}_i^{g,*}(t)\|, m_i \cdot b_f) \cdot \frac{\mathbf{F}_i^{g,*}(t)}{\|\mathbf{F}_i^{g,*}(t)\|} \end{cases} \tag{A.3}$$

where b_f (m/s^2) is the limit determining the maximum acceptable acceleration and m_i (kg) is the agent mass. The typical maximum acceleration of a human during normal movements is indeed limited, and this limitation is reproduced in the model by the parameter b_f, that needs to be calibrated. In this respect, Weidmann [73] reports that acceleration during normal walking does not typically exceed 1.96 (m/s^2) (0.2 g). In the social force model, however, social forces play also the role of braking forces, as they act to slow down agents when they need to avoid contacts with obstacles on their trajectory. Those kinds of situation, where a strong brake force is needed, cannot be considered as normal walking situations. For this reason it was considered more appropriate to use a value higher than 0.2 g, and the parameter b_f was set to 3 m/s^2. This value is also in line with the experimental data presented by Tirosh and Sparrow [68], where the situation of abrupt gait interruption is analysed. In addition to its relevance from the point of view of the underlying physics, the introduction of a bound on the force $\mathbf{F}_i^g$ has also a positive numerical effect, because it facilitate keeping accuracy in the integration of the equations of motion in case of increased time steps. This is extremely useful in case real time updating is required, and real-time application is one of the final scopes of the presented research activity (see also [47]).

The social torque is clamped, i.e. limited, in a similar way using a limiting value of angular acceleration (or torque per unit inertia), b_t (rad/s^2). Due the lack of data, b_t has been calibrated considering the maximum possible angular acceleration that can be generated by the motive torque (as reported later in (A.7)), which occurs when the agent is rotated backwards with respect to its preferred direction. The obtained value is $b_t = 62.83$ rad/s^2.

A.2. Characteristics of the agents

Each agent is associated with a set of characteristic properties which change from agent to agent. These properties can be grouped into geometrical, mechanical and behavioural properties.

Geometrical properties concern the way each agent is represented in the simulation. Each agent, corresponding to an evacuee in the simulation, has a defined shape and occupies a precise area that determines agents' interactions and collisions with obstacles and other agents. This shape must resemble the human shape as closely as

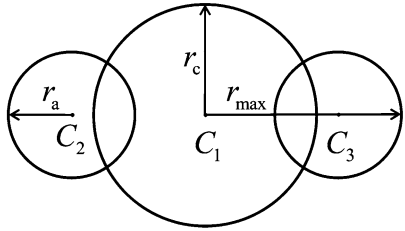

Fig. A.1. Agent geometry.

possible. A straightforward method of modelling the human geometry is by approximating a person's projected shape to a circle. However, this kind of simplification does not consider human asymmetry. To cope with this limitation, Helbing and Molnar [23] propose to model the human body with an ellipse. Unfortunately, using ellipses, which at first seem to be simple shapes, is actually computationally very onerous. Therefore, Korhonen [40] and Qu et al. [59] proposed to represent each evacuee with three circles (arms and chest). This kind of geometrical representation is still capable of considering human asymmetry and is also much less computationally expensive than the ellipse representation. As a result, this type of 3-circle representation is the one which has been selected for representing the area occupied by each agent in the present model.

Following Korhonen [40], each agent is represented by 3-circles having centre on the same line. The central circle models the chest while the lateral ones model the arms (Fig. A.1), and the geometry of the agent is globally determined by the maximum radius $r_{\max}$, the arm radius r_a and the chest radius r_c (Fig. A.1). Moreover, each agent is associated also with a total height h in the vertical direction.

The mass and the moment of inertia are the mechanical properties of each agent, and, following the idea by Korhonen [40] in the FDS+Evac code implementation, they are obtained by a scaling based on the agent's dimensions. In particular the scaling is carried out using three transformation coefficients for height (k_h), mass (k_m) and inertia (k_I). The values of these coefficients are set starting from to the reference case specified in FDS+Evac [40], where an agent of mass $m = 80$ kg is assumed to have inertia $I_Z = 4\ \text{kg} \cdot \text{m}^2$, $r_{\max} = 0.27$ m, $r_c = 0.16$ m and $h = 1.8$ m. Specifically, the scaling is carried out as follows:

$$\begin{cases} h = k_h \cdot r_{\max} \\ m = k_m \cdot r_{\max}^2 \\ I_z = k_I \cdot m \cdot (r_c^2 + r_{\max}^2) \\ \text{with} \\ k_h = (\frac{h}{r_{\max}})_{ref} = 6.67 \\ k_m = (\frac{m}{r_{\max}^2})_{ref} = 1097 \frac{kg}{m^2} \\ k_I = (\frac{I_z}{m \cdot (r_c^2 + r_{\max}^2)})_{ref} = 0.508 \end{cases} \tag{A.4}$$

Table A.2
Agent's dimensions

Agent type	$r_{\max}$ (m)	$r_c/r_{\max}$	$r_a/r_{\max}$
Adult	$U(0.22, 0.29)$	0.5882	0.3725
Male	$U(0.25, 0.29)$	0.5926	0.3704
Female	$U(0.22, 0.26)$	0.5833	0.3750

The way each agent interacts with the environment to reach its target is governed by the agent's properties and parameters. Most of those parameters are fixed and equal for all agents. Other parameters, are, instead, specified as random variables with associated distributions. In this latter category of parameters there are the unimpeded walking speeds (on flat terrain, while ascending and while descending stairs), the relaxation coefficient τ (for the motive force model) and the response time. The values of these parameters, which are typically modified in each random realization of the simulation, differ from one agent to another in such a way to reproduce the heterogeneity of the population. All random parameters contribute to the aleatory uncertainty inherent in the model.

For simulations in the maritime field, IMO MSC.1/Circ.1533 [32] provides information regarding the distribution of agents among different age/gender categories, of unimpeded speeds on flat terrain and on stairs, and of response time. However, no information is provided regarding the other agents' parameters which are required in the present model. Therefore, for parameters not addressed by IMO MSC.1/Circ.1533 [32], reference is made to the distributions specified by FDS+Evac [40], as reported in Table A.2. In the table the notation $U(a, b)$ indicates a uniform distribution in the interval $[a, b]$, and it can be noted that r_c and r_a are deterministically associated with $r_{\max}$ (for which the distribution is explicitly provided).

A.3. Motive force

The original motive force model by Helbing and Molnar [23] is based on the combined action of a propulsive force, which aims at reaching the desired speed in the desired direction, and a viscous friction component, which acts as a damper, as follows:

$$\mathbf{F}_i^{\text{mot}} = \frac{m_i}{\tau_i^f}\left(\mathbf{v}_i^0(t) - \mathbf{v}_i(t)\right) \tag{A.5}$$

where $\mathbf{v}_i^0(t)$ (m/s) is the instantaneous desired speed, $\mathbf{v}_i(t)$ (m/s) is the instantaneous speed, m_i (kg) is the mass of the agent and τ_i^f (s) is a relaxation coefficient determining the strength of the force. The instantaneous desired speed is associated with the routing algorithm, as described later in the relevant section.

It has been observed, both from literature [42] as well as from the initial simulations carried out with the original implementation of the presented model, that social repulsive forces may cause excessive acceleration that eventually induce unrealistic high speeds. In parallel, Tirosh and Sparrow [68] observed that, in human gait, peaks of breaking (decelerating) forces can be larger than peaks of accelerating forces. Therefore, starting from these considerations, the original motive force model (A.5) has been modified by introducing an additional term. The aim of the additional term is to generate larger friction, compared to the purely linear model (A.5), in case of large differences between the vectors of instantaneous actual and desired speed of an agent. The designed behaviour of the new model also handles the case of large instantaneous velocities. Such modification makes the new model for the motive force nonlinear. From a behavioural point of view, the new model is intended to represent the idea that agents increase their efforts in trying to recover the desired speed when they tend to be forced to move at velocities that are too different from the desired one. Furthermore, the modified model allows qualitatively reflecting the observations by Tirosh and Sparrow [68]. Compared to the original model (A.5), the new model has been devised in such a way not to impact on the behaviour of the original motive force in case of more standard conditions, characterised by acceleration from rest or low speed, or in case of small deviations from the desired speed.

The modified model takes the following form:

$$
\begin{cases}
\text{if } \|\delta\mathbf{v}_i(t)\| = 0: \quad \mathbf{F}_i^{\text{mot}}(t) = \mathbf{0} \\
\text{if } 0 < \|\delta\mathbf{v}_i(t)\| \leqslant s: \quad \mathbf{F}_i^{\text{mot}}(t) = \frac{m_i}{\tau_i^f} \cdot \|\delta\mathbf{v}_i(t)\| \cdot \delta\hat{\mathbf{v}}_i(t) \\
\text{if } \|\delta\mathbf{v}_i(t)\| > s: \\
\quad \mathbf{F}_i^{\text{mot}}(t) = \frac{m_i}{\tau_i^f} \cdot (\|\delta\mathbf{v}_i(t)\| + q_{\text{mot}} \cdot (\|\delta\mathbf{v}_i(t)\| \\
\qquad\qquad - k_{\text{mot}} \cdot v_i^0(t))) \cdot \delta\hat{\mathbf{v}}_i(t) \\
\text{where} \\
\delta\mathbf{v}_i(t) = \mathbf{v}_i^0(t) - \mathbf{v}_i(t); \qquad \delta\hat{\mathbf{v}}_i(t) = \frac{\delta\mathbf{v}_i(t)}{\|\delta\mathbf{v}_i(t)\|}; \\
s = k_{\text{mot}} \cdot v_i^0(t); \qquad q_{\text{mot}} > 0; \qquad k_{\text{mot}} > 1
\end{cases}
\tag{A.6}
$$

The dimensionless parameter q_{mot} controls the magnitude of the additional motive force when the modulus of the instantaneous speed difference $\delta\mathbf{v}_i(t)$ exceeds the specified threshold s governed by the dimensionless parameter k_{mot}. Herein, the two parameters have been tentatively set to $k_{\text{mot}} = 1.25$ and $q_{\text{mot}} = 3$. This means that the modified model is actually activated when $\|\mathbf{v}_i^0(t) - \mathbf{v}_i(t)\| > 1.25 \cdot v_i^0(t)$.

The parameter τ_i^f is often set to a value of 0.5 s [21,42]. However, a series of simulation tests carried out on the IMO test case 4 of MSC.1/Circ.1533 [32] showed that $\tau_i^f = 0.5$ s leads to excessive flow rate compared to the maximum one prescribed by MSC.1/Circ.1533 [32]. For this reason, the parameter τ_i^f was chosen to be uniformly distributed in the interval [0.8, 1.2] s, in accordance to the values proposed

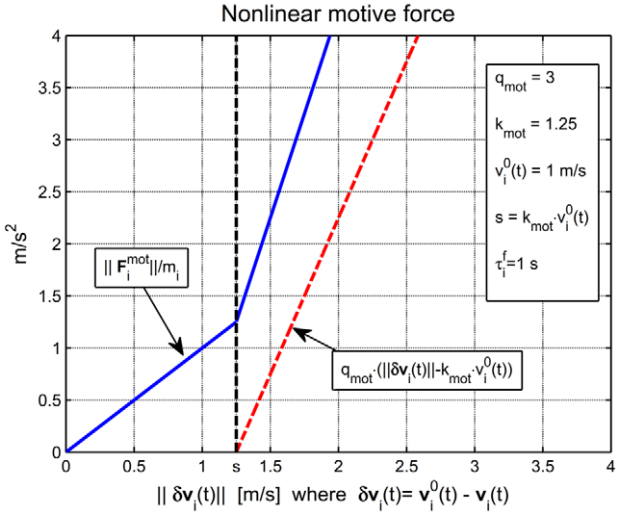

Fig. A.2. Example representative plot of nonlinear motive force behaviour.

by Korhonen [40]. While this is the reference model for the parameter τ_i^f to be associated as an agent's property, the instantaneous value of τ_i^f during a simulation can be modified, depending on the situation, by the nervousness model, as described later in Section A.8.

A representative plot of the behaviour of the nonlinear motive force with the considered model parameters is shown in Fig. A.2.

The motive torque describes the attitude of each agent to rotate towards its desired direction and it is described using the following model from Korhonen [40]:

$$T_i^{\text{mot}}(t) = \frac{I_i}{\tau_i^t} \cdot \left(\frac{(\phi_i^0(t) - \phi_i(t))}{\pi} \cdot \omega^0 - \omega_i(t) \right) \tag{A.7}$$

where $\phi_i^0(t)$ (rad) is the instantaneous desired orientation angle, $\phi_i(t)$ (rad) is the instantaneous orientation angle (defined in $[-\pi, \pi]$), $\omega_i(t)$ (rad/s) is the instantaneous angular speed, τ_i^t (s) is the relaxation parameter of the motive torque, and ω^0 (rad/s) is a scaling parameter. While τ_i^t controls directly the viscous dissipation of the model, the parameter ω^0, combined with τ_i^t, controls the restoring term of the motive force. According to the approach used in FDS+Evac [40], the relaxation parameter τ_i^t is herein assumed to scale with τ_i^f so that $\tau_i^t = k_\tau \cdot \tau_i^f$ where k_τ is a fixed parameter. In line with Korhonen [40], k_τ was set to 0.2 s and ω^0 was set to 4π rad/s.

Finally, the parameters associated with the motive force and motive torque models are summarized in Table A.3.

Table A.3
Parameters of motive force and motive torque models, and corresponding values

τ_i^f	q_{mot}	k_{mot}	τ_i^t	k_τ	ω^0
$U(0.8s, 1.20s)$	3	1.25	$k_\tau \cdot \tau_i^f$	0.2	4π rad/s

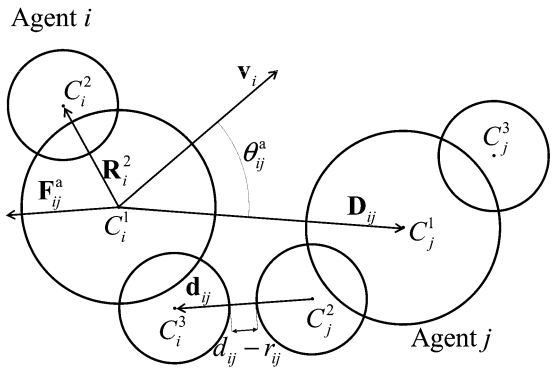

Fig. A.3. Agent-agent interaction.

A.4. Agent-agent interaction

The repulsive interaction force between agents models the way people try to avoid contacts and keep distance. This force was firstly introduced by Helbing and Molnar [23]. However, herein, the FDS+Evac model by Korhonen [40] is implemented, as this latter is based on the three circle representation of the human body. That model is also slightly modified here, in order to better address the case of zero agent speed.

With reference to the geometrical scheme reported in Fig. A.3, the force exerted on agent i by agent j is described as follows:

$$\mathbf{F}_{ij}^a(t) = A_i^a(t) \cdot e^{-\left(\frac{d_{ij}-r_{ij}}{B_a}\right)} \cdot \left(\lambda_a\big(v_i(t)\big) + \big(1-\lambda_a\big(v_i(t)\big)\big) \cdot \left(\frac{1+\cos(\theta_{ij}^a)}{2}\right)\right) \cdot \widehat{\mathbf{d}_{ij}} \tag{A.8}$$

where $d_{ij} - r_{ij}$ is the effective (skin-to-skin) distance between the closest agents' circles, $\widehat{\mathbf{d}_{ij}}$ is the versor of the vector $\mathbf{d}_{ij}$ connecting the centres of closest circles (oriented from agent j to agent i), θ_{ij}^a is the angle between the instantaneous speed $\mathbf{v}_i(t)$ of agent i and the vector $\mathbf{D}_{ij}$ connecting the two agents' centres (from agent i to agent j).

The coefficient $A_i^a(t)$ (N), is, in general, time dependent, because, according to the FDS+Evac model [40], it is described as follows:

$$A_i^a(t) = A_a \cdot \max\left(0.5, \frac{v_i(t)}{v_i^0(t)}\right) \tag{A.9}$$

where A_a (N) is a fixed constant, and $v_i(t)$ and $v_i^0(t)$ are, respectively, the modulus of the instantaneous speed and the modulus of the desired speed. The parameter A_a determines the strength of the force. In order to set the value for this parameter, reference was made to the value used by Helbing et al. [21], i.e. $A_a = 2 \cdot 10^3$ N. As Lakoba et al. [42] correctly observe, using this value for the A_a parameter might lead to forces far from being realistic. In the model presented herein, however, this issue is indirectly addressed by the clamping procedure described in (A.3), as it is understood that the agent-agent interaction force, when considered in isolation, is to be intended more as an indication of an intention from the agent rather than, strictly, as a physical force.

The parameter B_a controls the decay of the force as a function of the relative agent's distance, and, according to Helbing et al. [21], it is set to $B_a = 0.08$ m. Considering the exponential decay associated to B_a, this clarifies that the agent-agent interaction is a close-distance type of interaction, and it can be neglected when agents are sufficiently far from each other. From a computational perspective, this is an extremely important factor in a model that targets a real-time application, as in this case. In fact, in principle, given a simulation with N agents where all agents are visible to each other, a total of $N \cdot (N-1)$ agent-agent interactions should be computed at each time step. By neglecting agents that are at a sufficiently large distance from each other compared to the decay scale B_a, the agent-agent interactions can be computed only for agents in relatively close proximity. This eventually avoids the $\sim N^2$ scaling of computational time for the agent-agent interaction. Instead, qualitatively, the computational time tends to increase in a way that is closer to a linear dependence on the number simulated agents ($\sim N$), depending on the average number of agents that are in close proximity, i.e. depending on the average density for the specific case under analysis. Higher densities lead to a larger number of agents in close proximity, and this increases the number of calculated agent-agent interactions, hence the computational time. Conversely, lower densities reduce the average number of agents in close proximity, hence the computational time associated with the determination of agent-agent interactions.

The second part of equation (A.8) concerns the anisotropy of agent-agent interaction, and it is controlled by the parameter λ_a. In general, it is assumed that the agent-agent interaction force is larger if the agent j is placed in front of the instantaneous direction of agent i and, conversely, it is smaller when agent j is placed behind the instantaneous direction of agent i. This corresponds, in general, to an anisotropy parameter $0 \leqslant \lambda_a < 1$, with the model anisotropy increasing for smaller values of λ_a. However, in case $v_i(t) = 0$ (idle agent) the angle θ_{ij}^a is not defined. Korhonen [40] assumed in their model that idle agents have an increased perception of the other agents around them, and therefore no anisotropy is applied to them ($\lambda_a = 1$). While this observation can be considered reasonable, this choice makes the interaction force discontinuous with respect to the angle θ_{ij}^a whenever any anisotropy is assumed in the presence of an agent speed ($\lambda_a \neq 1$). In order to address this minor

issue, the model presented herein considers a weak dependence of the anisotropy parameter on the modulus of the instantaneous agent's speed $v_i(t)$. In particular, λ_a is taken equal to 1.0 when $v_i(t) = 0$, it is taken equal to the nominal value (discussed later) when $v_i(t) \geqslant 0.01$ m/s, and it is linearly interpolated for intermediate values of $v_i(t)$. Eventually, this modification leads to a force which is defined with continuity and avoids oscillation near $v(t) = 0$, and, at the same time, it does not drastically modify agents' behaviour in comparison with the original modelling by Korhonen [40].

Regarding the actual value of the anisotropy parameter λ_a, different alternatives have been proposed in literature. Johansson et al. [38] suggested $\lambda_a \approx 0.1$ following a parameter identification technique, using evolutionary optimization, based on video recorded data. In FDS+Evac [40] a standard value $\lambda_a = 0.3$ is used, with an indication that this value can be increased to 0.5 in case a faster egress is required. Liao et al. [43] performed a calibration study regarding the anisotropy parameter λ_a in FDS+Evac model, observing that the increase of the parameter λ_a up to 0.5 allows obtaining a flow rate which is closer to experimental results. With reference to the application to the maritime field, which is the target of this study, preliminary simulations with the presented model indicated that considering $\lambda_a = 0.5$ led to a flow rate in the IMO test case 4 larger than the imposed IMO limit of 1.33 p/s. Therefore, eventually, a value $\lambda_a = 0.3$ has been chosen as the default parameter for the model presented herein, since this value seemed more appropriate for the purpose of studying a situation of ordered evacuation in line with the requirements of IMO. More experimental results are however needed to properly determine this coefficient and its possible dependencies on the detailed characteristics of the evacuation condition.

In parallel to the agent-agent interaction force, the agent-agent interaction model considers also the effect of a torque. In particular, the torque models the way people rotate their body in order to avoid contacts. The agent-agent interaction torque is not directly generated by the interaction force, which is, instead, considered to be applied in the centre of mass of the agent.

The torque exerted by agent j on agent i is expressed as follows:

$$\mathbf{T}_{ij}^{a}(t) = \max_{h\in\{1,2,3\}} \left(\mathbf{R}_i^2 \times \mathbf{F}_{ij}^{2h}\right) + \max_{h\in\{1,2,3\}} \left(\mathbf{R}_i^3 \times \mathbf{F}_{ij}^{3h}\right) \tag{A.10}$$

Where, with reference to Fig. A.3, $\mathbf{R}_i^k$ is the vector connecting the agent centre $\mathbf{C}_i^1$ to the arm centre $\mathbf{C}_i^k$. $\mathbf{F}_{ij}^{kh}$ is the virtual force calculated from equation (A.8) by considering, however, the circle centres $\mathbf{C}_i^k$ and $\mathbf{C}_j^h$, instead of the closest circle centres. The force $\mathbf{F}_{ij}^{kh}$ is, thus, directed as the vector $\mathbf{d}_{ij}^{kh}$ connecting the two centres.

Finally, the resulting agent-agent interaction force and torque exerted on agent i are given by the summation of the contribution from all interacting agents j, i.e.

$$\begin{cases} \mathbf{F}_i^a(t) = \sum_{j \text{ interacting}} \mathbf{F}_{ij}^a(t) \\ \mathbf{T}_i^a(t) = \sum_{j \text{ interacting}} \mathbf{T}_{ij}^a(t) \end{cases} \tag{A.11}$$

Table A.4
Parameters of agent-agent interaction model, and corresponding values

A_a	λ_a		B_a
$2 \cdot 10^3$ N	$\begin{cases} 1.0 \\ 1 - 70 \cdot v_i(t) \\ 0.3 \end{cases}$	for $v_i(t) = 0$ m/s for 0 m/s $< v_i(t) <$ 0.01 m/s for $v_i(t) \geqslant$ 0.01 m/s	0.08 m

Agents do not interact when a wall is placed between them, i.e. when they are not visible each other. To this end, a corresponding visibility check between agents i and j is carried out during the simulation: if the segment connecting the centres of agents intersects the mesh representing the environment, the two agents are considered not to be visible to each other. Moreover, considering the exponential spatial decay in the interaction effects (see (A.8)), agents are considered to be non-interacting when their skin-to-skin distance exceeds $10 \cdot B_a$. This last check allows a significantly reduced computational time in case of simulations with a large number of agents, by reducing the number of agents to be taken into account in the calculation of the agent-agent interaction force at each time step.

A summary of parameters associated with the agent-agent interaction model is reported in Table A.4.

A.5. Agent-wall interaction

The repulsive interaction force between agents and walls (obstacles in general) models the way people try to avoid contacts with, and keep distance from, obstacles and walls. In the present model walls and obstacles are considered as three dimensional objects modelled by appropriate triangular meshes. The agent-wall interaction force is determined on the basis of the distance between the agent and the closest point on the geometrical mesh. Moreover, the model can deal with generic shapes of the walls and obstacles, making it very flexible also in case of complex walls/obstacles geometries which, therefore, do not need strong modelling simplifications.

Starting from, and modifying, the background from Helbing and Molnar [23] and Korhonen [40], the model for the agent-wall interaction force is very similar to the single agent-agent interaction force model (A.8), and it is described as follows (see Fig. A.4):

$$\mathbf{F}_i^w = A_i^w(t) \cdot e^{-\left(\frac{d_i - r_i}{B_w}\right)} \cdot \left(\lambda_w\big(v_i(t)\big) + \big(1 - \lambda_w\big(v_i(t)\big)\big) \cdot \left(\frac{1 + \cos(\theta_i^w)}{2}\right)\right) \cdot \widehat{\mathbf{d}}_i \tag{A.12}$$

where $\widehat{\mathbf{d}}_i$ is the versor corresponding to the distance vector $\mathbf{d}_i$ connecting the centre of the closest circle to the wall closest point, $d_i - r_i$ is the corresponding skin-to-wall distance, and θ_i^w is the angle between the instantaneous agent speed $\mathbf{v}_i(t)$ and

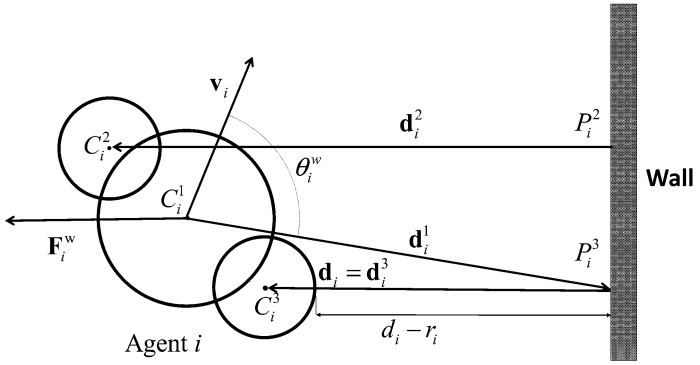

Fig. A.4. Agent-wall interaction.

the vector $\mathbf{d}_i^1$ connecting the agent's centre to the closest reference point on the wall. Also in this case, similarly to the case of agent-agent interaction, the magnitude of the force is controlled by a, possibly time dependent, parameter $A_i^w(t)$ (N), which is assumed to have the same speed dependence as in (A.9), using a reference value $A_w = A_a = 2 \cdot 10^3$ N. The anisotropy is controlled by the weakly speed dependent dimensionless parameter $\lambda_w(v_i(t))$, where the speed dependence is modelled exactly as in case of the agent-agent interaction. However, taking into account Korhonen et al. [41], a reference value $\lambda_w = 0.2$ for non-(almost)idle agents, is assumed. The decay of the force as the net distance from the wall increases is controlled by the spatial scale parameter B_w (m) which is taken as $B_w = 0.04$ m.

The agent-wall interaction torque is modelled as the sum of two contributions, which can be considered as the torques associated with each agent arm, as follows:

$$\mathbf{T}_i^w = \left(\mathbf{R}_i^2 \times \mathbf{F}_i^2\right) + \left(\mathbf{R}_i^3 \times \mathbf{F}_i^3\right) \tag{A.13}$$

where, with reference to Fig. A.4 and for $h \in \{2, 3\}$ (left and right arm, respectively), $\mathbf{R}_i^h$ is the vector connecting the agent centre to the centre $\mathbf{C}_i^h$ and $\mathbf{F}_i^h$ is a force calculated according to (A.12), but using different variables which are associated with the considered agent arm. The direction of the force $\mathbf{F}_i^h$ is the direction of vector $\mathbf{d}_i^h$ connecting the point $\mathbf{P}_i^h$ (the wall closest point from the centre $\mathbf{C}_i^h$) to the centre $\mathbf{C}_i^h$ (note the opposite defined orientation between $\mathbf{d}_i^1$ and $\mathbf{d}_i^2$, $\mathbf{d}_i^3$). The considered effective distance is the one between the wall and the circle centred $\mathbf{C}_i^h$. The anisotropic component is calculated using an angle θ_i^h between the instantaneous agent and velocity $\mathbf{v}_i(t)$ and the vector $-\mathbf{d}_i^h$.

A summary of parameters associated with the agent-wall interaction model is reported in Table A.5.

Table A.5
Parameters of agent-wall interaction model, and corresponding values

A_w		λ_w	B_w
$2 \cdot 10^3$ N	$\begin{cases} 1.0 \\ 1 - 80 \cdot v_i(t) \\ 0.2 \end{cases}$	for $v_i(t) = 0$ m/s for 0 m/s $< v_i(t) <$ 0.01 m/s for $v_i(t) \geqslant$ 0.01 m/s	0.04 m

A.6. Counter-flow

Agent-agent repulsive force/torque alone cannot properly model the behaviour of pedestrians in situations of counter-flow, i.e. in those situations where agents have opposite (or different) directions. In such cases, a model is required that is specifically suited to induce the lateral shift which is typically performed by pedestrians in order to avoid incoming people.

Different studies have been carried out in relation to the counter-flow situation (e.g. [35,77]), which highlighted recurring patterns in experiments. The most observed pattern is the lane formation: people tend to form separated lanes, and this configuration tends to maximize the flow rate, as it is reported by Zhang et al. [77].

Two main approaches can be identified from the existing literature on how to integrate counter-flow models in the social force modelling. One approach is based on the modelling of the counter-flow as an additional force component, as suggested by Guo [18] and by Pelechano et al. [56]. Instead, in the alternative approach, the response to a counter-flow situation is modelled through a modification of the agent's instantaneous desired speed, as described by Heliövaara et al. [26].

Herein, a newly developed model is presented. The model is a short-range one, describing the pedestrian reaction to a counter-flow situation through an additional force, i.e. in line with the former of the two approaches described above. Conceptually in line with the agent-agent interaction model, for a considered agent, the interactions with each incoming agent in a counter-flow condition are considered separately, and the individual contributions are then summed up.

In the presented model, for the considered agent, the classification of whether any other incoming agent is in counter-flow is based only on instantaneous physically observable variables, such as the instantaneous speed, the body orientation and the position of the incoming pedestrian.

First, with reference to Fig. A.5 and Fig. A.6, the following quantities $p_1 p_2$ and p_3 are defined:

$$p_1 = \left\langle \widehat{\mathbf{v}}_i^0, \widehat{\mathbf{D}}_{ij} \right\rangle = \cos(\theta_{ij}) \tag{A.14}$$

$$p_2 = -\left\langle \widehat{\mathbf{v}}_i^0, \widehat{\mathbf{n}}_j \right\rangle = -\cos(\eta_{ij}) = \cos(\pi - \eta_{ij}) \tag{A.15}$$

$$p_3 = f\left(v_{ij}^{r0}\right) \tag{A.16}$$

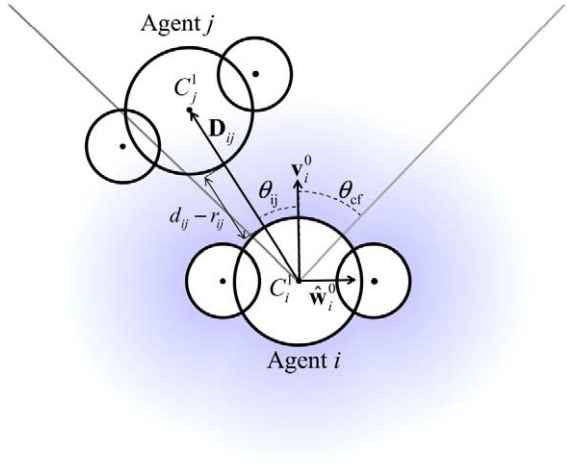

Fig. A.5. Example of counter-flow situation when considering only conditions (A.19) and (A.20).

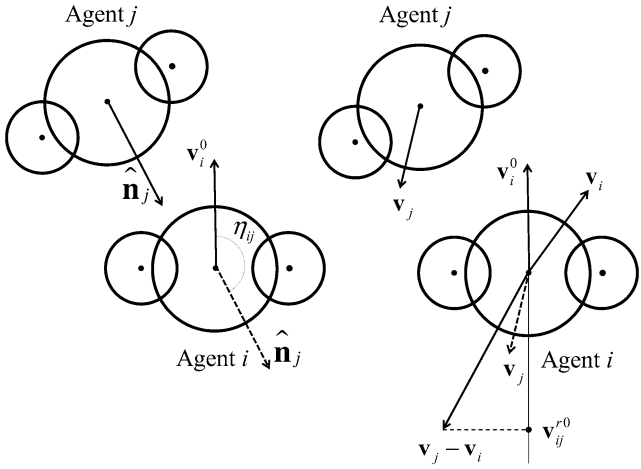

Fig. A.6. Examples of counter-flow situation when considering only conditions (A.21) (left) and (A.22) (right).

where the $\langle \cdot, \cdot \rangle$ operator indicates the dot product, $\widehat{\mathbf{v}}_i^0$ is the versor of agent i desired speed vector $\mathbf{v}_i^0$, $\widehat{\mathbf{D}}_{ij}$ is the versor of the vector $\mathbf{D}_{ij}$ connecting agents centres, $\widehat{\mathbf{n}}_j$ is the orientation vector of agent j (pointing towards the front direction of the agent). The function $f(v_{ij}^{r0})$ depends on the component, along the direction $\widehat{\mathbf{v}}_i^0$, of the relative

speed of agent j with respect to agent i, as follows:

$$\begin{cases} v_{ij}^{r0} = \langle \widehat{\mathbf{v}}_i^0, (\mathbf{v}_j - \mathbf{v}_i) \rangle \\ f(v_{ij}^{r0}) = \begin{cases} 1 & \text{for } v_{ij}^{r0} < 0 \\ 1 - \frac{v_{ij}^{r0}}{V_i^{\text{cf}}} & \text{for } 0 \leqslant v_{ij}^{r0} \leqslant V_i^{\text{cf}} \\ 0 & \text{for } v_{ij}^{r0} > V_i^{\text{cf}} \end{cases} \end{cases} \tag{A.17}$$

The reference speed V_i^{cf} (m/s) is defined as a function of the unimpeded walking speed v_i^{u}, which is a specific characteristic of each agent, i.e.

$$V_i^{\text{cf}} = k_{\text{cf}} \cdot v_i^u \tag{A.18}$$

An agent j is defined to be in counter-flow with respect to the considered agent i, when all the following conditions are fulfilled:

$$p_1 \geqslant \cos(\theta_{\text{cf}}) \tag{A.19}$$

$$d_{ij} - r_{ij} < D_{\text{cf}} \tag{A.20}$$

$$p_2 > 0 \tag{A.21}$$

$$p_3 > 0 \tag{A.22}$$

Conditions (A.19) and (A.20) refer to the relative position of agent j with respect to agent i, taking into account this latter's desired velocity. A counter-flow condition is potentially identified only if agent j is positioned within an angular sector of amplitude θ_{cf} around the direction identified by $\widehat{\mathbf{v}}_i^0$ (see (A.19)), and, in addition (see (A.20)), agent j is also closer to agent i than a cut-off distance D_{cf}, considering the effective skin-to-skin distance $d_{ij} - r_{ij}$ between the closest circles among agents. A graphical representation is shown in Fig. A.5.

The condition (A.21) identifies a potential counter-flow situation on the basis of the angle between the desired speed of agent i and the orientation of agent j, and this condition prevents from considering, for instance, agents in a queue as being in a counter-flow situation. Finally, condition (A.22) identifies potential counter-flow situation using the component of the relative velocity of agent j with respect to agent i along the direction of the desired speed of agent i. In particular, through (A.17), agent j is identified as being potentially in counter-flow whenever such component is strictly negative or, alternatively, positive, but smaller than the threshold V_i^{cf} (see (A.18)). This latter case allows to properly identify counter-flow situations also in those conditions, typically corresponding to low speed, when the agents are facing each other and the agent j is moving backward. Allowing the counter-flow to be triggered also when the relative speed is slightly positive is necessary in order to apply the counter-flow force with continuity in situations of high crowd density. Indeed, in

these situations, due to interaction forces, it was observed that agents might sometimes have velocities with opposite direction with respect to their desired ones. In such conditions, without the introduction of the threshold $V_i^{\mathrm{cf}}(>0)$ in (A.17)/(A.22), the counter-flow model would randomly be triggered on and off. Conditions (A.21) and (A.22) are exemplified in Fig. A.6.

When the agent j is identified to be in counter-flow with respect to agent i, the modulus of its contribution to the counter-flow force on agent i is modelled as follows:

$$\left\|\mathbf{F}_{ij}^{\mathrm{cf}}\right\| = A_{\mathrm{cf}} \cdot \left(1 - \frac{d_{ij} - r_{ij}}{D_{\mathrm{cf}}}\right) \cdot \left(\left(\frac{p_1 - \cos(\theta_{\mathrm{cf}})}{1 - \cos(\theta_{\mathrm{cf}})}\right) \cdot p_2\right)^{\alpha_{\mathrm{cf}}} \cdot p_3 \tag{A.23}$$

Whenever a counter-flow condition is identified, the model for $\|\mathbf{F}_{ij}^{\mathrm{cf}}\|$ is continuous with respect to all the dependent variables, and $\|\mathbf{F}_{ij}^{\mathrm{cf}}\|$ decreases to 0 as any of the counter-flow conditions (A.19)- (A.22) is not satisfied. The numerical values selected for the various parameters for the determination of $\|\mathbf{F}_{ij}^{\mathrm{cf}}\|$ are described in the following.

The threshold speed V_{cf} in (A.17) has tentatively been fixed to 10% of unimpeded agent speed v_i^{U}, i.e. $k_{\mathrm{cf}} = 0.10$ in (A.18), because, from preliminary simulations, this value allowed to provide realistic outcomes in case of counter-flow situations characterised by high density.

The numerical specification of θ_{cf} and D_{cf} corresponds, basically, to the specification of the region of positioning of agent j with respect to agent i within which the counter-flow model can be triggered (shortly, the "counter-flow region"), and this is fundamental to identify a potential counter-flow condition. The counter-flow region defined by Heliövaara et al. [26] is roughly elliptical, extending 3 m ahead of agent i and up to 1.5 m on its sides. The same maximum extents have been used by Pelechano et al. [56], but with a counter-flow region having a rectangular shape. The implicit counter-flow region considered for the model presented herein is defined considering the skin-to-skin distance $d_{ij} - r_{ij}$, and takes into account, therefore, the actual agents' dimensions. The threshold distance D_{cf} at which the model is triggered has been tentatively fixed to 2 m. This value appeared reasonable for the short-range nature of the model and in line with the indications available in literature. Regarding the parameter θ_{cf}, which, in the present model, characterises the half width of the angular sector within which agent j needs to be in order for being considered in a potential counter-flow condition, its value was tentatively set to 45°. This value was set by means of preliminary calculations and also taking into account that, in the model by Heliövaara et al. [26], an agent tends to proceed undisturbed when there are no agents in counter-flow in a frontal sector with a width of around $\pm 40° \div \pm 45°$.

The strength of the counter-flow force depends on the parameter A_{cf} (N) which requires a calibration. A first calibration of this parameter has been made using IMO test case 8 reported in MSC.1/Circ.1533 [32] and experimental data provided by Isobe et al. [35]. The calibration also addressed the exponent α_{cf} which is another

characteristic parameter of the proposed model. The parameter α_{cf} controls the level of interaction with lateral agents and with agents not fully oriented towards $\widehat{\mathbf{v}}_i^0$. Reducing the value of α_{cf} increases the force originated by interaction with agents placed laterally or agents not in front of the desired direction of agent i. A good agreement with experimental data by Isobe et al. [35] was obtained with $A_{cf} = 225$ N and $\alpha_{cf} = 1/3$.

Equation (A.23) provides the modulus of the counter-flow force exerted by agent j on agent i. Regarding its direction, the force is, as a basis, perpendicular to the direction of the desired speed $\widehat{\mathbf{v}}_i^0$, since it is intended to model a lateral shift. However, its orientation (right or left with respect to $\widehat{\mathbf{v}}_i^0$), depends on the relative position of agent j in counter-flow with respect to agent i. In general, agents tend to move in the direction opposite to that where the counter-flow agent is coming from. It has been observed that, in most cultures, there exists a preferred direction for pedestrian traffic which, usually, improves the organization of opposite flows in counter-flow conditions (e.g. [26,75]). In order to reproduce this behaviour, in the presented model this preference is expressed by the introduction of an offset angle parameter η_{cf}. In particular, the versor of the counter-flow force is defined as follows:

$$\hat{\mathbf{F}}_{ij}^{cf} = -1 \cdot \mathrm{sign}\left(\left\langle \hat{\mathbf{w}}_i^0, \hat{\mathbf{D}}_{ij} \right\rangle - \sin(\eta_{cf})\right) \cdot \hat{\mathbf{w}}_i^0 \tag{A.24}$$

where $\hat{\mathbf{w}}_i^0$ is the unit vector oriented from the centre to the right arm of agent i. In case $\eta_{cf} = 0$ there is no preferred direction and the model is symmetrical. According to (A.24), and with reference to Fig. A.5, the counter-flow force will have the same direction as $\hat{\mathbf{w}}_i^0$ if $\vartheta_{ij} \leqslant \eta_{cf}$ and will have opposite direction otherwise. It is also worth underlining that the preferred direction is on the right with respect to the desired speed of agent i if η_{cf} is positive, whereas it is on the left if η_{cf} is specified as negative. Herein, the preferred direction parameter has been tentatively set to $\eta_{cf} = 12°$, and this value was set in order to obtain a reasonable reproduction of experimental data from Isobe et al. [35] without introducing a too strong right preference.

Eventually, the contribution to the counter-flow force vector due to agent j is determined by combining (A.23) and (A.24):

$$\mathbf{F}_{ij}^{cf} = \left\| \mathbf{F}_{ij}^{cf} \right\| \cdot \hat{\mathbf{F}}_{ij}^{cf} \tag{A.25}$$

In addition to a translational shifting, which is induced by the counter-flow force, also a counter-flow-induced rotation needs to be modelled. In fact, Heliövaara et al. [26] observed that in counter-flow conditions people change their body orientation in order to better fit in narrow spaces, moving shoulder first. This behaviour is fundamental for models, as the present one, representing the human body with its asymmetry, particularly in high-density counter-flow conditions. In the model presented

herein, the described behaviour is modelled with a counter-flow torque contribution induced by agent j on agent i, having modulus as follows:

$$\left\|\mathrm{T}_{ij}^{\mathrm{cf}}\right\| = A_{\mathrm{cft}} \cdot \left(1 - \frac{d_{ij} - r_{ij}}{D_{\mathrm{cft}}}\right) \cdot \left(\left(\frac{p_1 - \cos(\theta_{\mathrm{cf}})}{1 - \cos(\theta_{\mathrm{cf}})}\right) \cdot p_2\right)^{\alpha_{\mathrm{cf}}} \cdot p_3 \tag{A.26}$$

The previous expression differs from that used for the modulus of the counter-flow force (A.23) only in the characteristic parameters A_{cft} ($N \cdot$ m) and D_{cft} (m).

The counter-flow torque model needs to be activated at a closer distance compared to the counter-flow force model, as the change of orientation of pedestrians typically happens only if people are very close each other. As a result, the spatial scale parameters D_{cft} was tentatively set to 1 m, i.e. half of D_{cf}. Moreover, from preliminary calibration simulations a value $A_{\mathrm{cft}} = 30$ N $\cdot$ m was set, since it was observed that higher values of A_{cft} caused unnaturally fast rotations.

The direction of the torque, which eventually governs the direction of agent i rotational acceleration, is determined by the direction of the force as follows:

$$\hat{\mathbf{T}}_{ij}^{cf} = \mathrm{sign}\left(\left\langle \hat{\mathbf{w}}_i^0, \hat{\mathbf{F}}_{ij}^{\mathrm{cf}} \right\rangle\right) \cdot \hat{\mathbf{z}} \tag{A.27}$$

where $\hat{\mathbf{z}}$ is the versor of the vertical axis. Eventually, the torque contribution due to agent j is determined by combining (A.26) and (A.27):

$$\mathbf{T}_{ij}^{\mathrm{cf}} = \left\|\mathbf{T}_{ij}^{\mathrm{cf}}\right\| \cdot \hat{\mathbf{T}}_{ij}^{\mathrm{cf}} \tag{A.28}$$

The total counter-flow force and torque vectors are determined by summing up the contributions from all agents identified to be in counter-flow:

$$\begin{cases} \mathbf{F}_i^{\mathrm{cf}}(t) = \sum_{j \text{ in counter-flow}} \mathbf{F}_{ij}^{\mathrm{cf}}(t) \\ \mathbf{T}_i^{\mathrm{cf}}(t) = \sum_{j \text{ in counter-flow}} \mathbf{T}_{ij}^{\mathrm{cf}}(t) \end{cases} \tag{A.29}$$

From a series of preliminary calibrations, it was observed that this model may generate impasse situations, particularly in the case of bottlenecks. In order to avoid such situations, a random variation of direction of the force $\mathbf{F}_i^{\mathrm{cf}}(t)$ is implemented, in such a way that the force does not remain exactly parallel to $\hat{\mathbf{w}}_i^0$. Therefore, to this end, the force $\mathbf{F}_i^{\mathrm{cf}}(t)$, while keeping the same modulus as in (A.29), is oriented by an angle $\delta\psi(t)$ with respect to the nominal direction obtained by (A.29). The time history of angle $\delta\psi(t)$ is generated according to the same procedure described hereinafter for the random forces, within a range $[-\delta\psi_{\mathrm{cf}}, \delta\psi_{\mathrm{cf}}]$. Following preliminary calibrations a value $\delta\psi_{\mathrm{cf}} = 15°$ was tentatively set.

It is also noted that, similarly to the case of agent-agent interaction, the possible counter-flow interaction is considered only if agent j is visible to agent i, and the same visibility check used for agent-agent interaction forces is also applied in the case of counter-flow interaction.

Table A.6
Parameters of counter-flow model, and corresponding values

D_{cf}	D_{cft}	A_{cf}	A_{cft}	θ_{cf}	η_{cf}	V_i^{cf}	k_{cf}	α_{cf}	$\delta\psi_{cf}$
2 m	1 m	225 N	30 N · m	45°	12°	$k_{cf} \cdot v_i^u$	0.1	$\frac{1}{3}$	15°

Finally, a summary of the parameters associated with the counter-flow model is reported in Table A.6.

A.7. Random fluctuations

As anticipated in the description of the various force contributions, some random fluctuation is added to several terms. In particular, random forces and random torque are directly applied to each agent. Moreover, random fluctuations are also applied to the angle of the counter-flow force. The role of the random noise is twofold. On the one hand it mimics a certain level of inherent natural randomness in the agents' behaviour. On the other hand, the addition of a random noise also prevents the occurrence of unnatural impasse situations (equilibria of the dynamical system), which, in real cases, are typically resolved by interactions between pedestrians. However, large magnitudes of random forces can have the opposite effect, by creating impasse situations through so-called "freezing by heating effect" [24].

In the developed tool, random fluctuations are all generated using the same type of algorithm. The idea underlying the algorithm is based on the FDS+Evac code implementation [40], since this very well fits the idea of using the tool also in real-time without predetermined duration of the simulation.

The time history of a generic stochastic process $X(t)$, for which a distribution is specified, is generated starting from an initial randomly generated value $x_0 = x$ ($t = 0$ s). Then, given a first time step Δt_1, the random variable X at $t = \Delta t_1$, i.e. x_1, is kept the same as x_0 with probability $P_S(\Delta t_1)$, or updated with a new independent value sampled from the same distribution with probability $1 - P_S(\Delta t_1)$. The same is repeated for all the subsequent time steps Δt_i ($i = 2, 3, \ldots$), independently from the previous ones, and it allows to generate, in real-time, the discrete time history x_i ($i = 0, 1, 2, \ldots$). It is also noted that the time step can be, in general, a variable time step. In order to guarantee that, from a statistical perspective, the procedure is independent from the chosen simulation time step, the probability $P_S(\Delta t)$ is taken as follows:

$$P_S(\Delta t) = e^{-\alpha \cdot \Delta t} \tag{A.30}$$

where α (s^{-1}) is a specified time constant. By determining the autocorrelation function of the process, and taking its Fourier transform, it can be proved that the stochastic process $X(t)$ resulting from the described procedure, after removing its mean, has

a single-side power spectral density as follows:

$$S(\omega) = \frac{\sigma^2}{\pi} \cdot \frac{2 \cdot \alpha}{\omega^2 + \alpha^2} \tag{A.31}$$

where σ^2 is the variance of the process and ω (rad/s) is the circular frequency. The obtained result is independent on the actual instantaneous distribution of X, and the power spectral density $S(\omega)$ is directly proportional to the variance of the process. Expression (A.31) allows to select the time constant α having a clear view of its effect on the energy distribution of the resulting process in the frequency domain. In addition, the knowledge of the theoretical spectrum (A.31) of the process, allows to select α in order to reduce aliasing effects which inevitably occur in simulations with discrete time steps.

Random forces are conventionally generated, for each agent, by separately generating the force modulus R_F and the orientation ϑ_F of the force in the simulation reference system. While the distributions for the two variables are different, the update of the variables according to the random procedure specified above is done at the same time for both variables, i.e. the two variables are either updated or not updated at a generic time instant during the simulation. As a result, the update of the two variables is based on a common parameter α_F. The components of the force are then determined as:

$$\begin{cases} F_x^{\text{rand}} = \cos(\theta_F) \cdot R_F \\ F_y^{\text{rand}} = \sin(\theta_F) \cdot R_F \end{cases} \tag{A.32}$$

The distribution selected for R_F is a truncated Rayleigh, while a uniform distribution $U(0, 2\pi)$ is selected for ϑ_F, and the two variables are statistically independent. As a result, the components F_x^{rand} and F_y^{rand} are approximately (due to the truncation of the Rayleigh distribution) Gaussian and independent. The expression for the distribution of R_F is:

$$\begin{cases} \text{pdf}(R_F) = \frac{R_F}{C_F \cdot b_F^2} \cdot \exp(-\frac{R_F^2}{2 \cdot b_F^2}) \\ C_F = 1 - \exp(-\frac{R_{F,\max}^2}{2 \cdot b_F^2}) \\ R_{F,\max} = k_{rf} \cdot b_F \\ R_F \in [0,\, R_{F,\max}] \end{cases} \tag{A.33}$$

To avoid the possibility of too large random forces due to the tails of the Rayleigh distribution, the truncation is taken at $k_{rf} = 4$. The parameter b_F in (A.33) is indirectly determined by specifying the desired standard deviation σ_{rf} of each force component in (A.32) and noting that, from (A.32) and the selected distribution for

ϑ_F, the random variables F_x^{rand} and F_y^{rand} are both zero mean and independent. Then, it follows that:

$$E\left\{\left(F_x^{\text{rand}}\right)^2 + \left(F_y^{\text{rand}}\right)^2\right\} = 2 \cdot \sigma_{rf}^2 = E\left\{R_F^2\right\}$$

$$\Rightarrow \quad b_F = \sigma_{rf} \cdot \sqrt{\frac{1 - \exp(-\frac{k_{rf}^2}{2})}{1 - \exp(-\frac{k_{rf}^2}{2}) \cdot (1 + \frac{k_{rf}^2}{2})}} \tag{A.34}$$

The standard deviation σ_{rf} is set proportionally to the mass m_i of each agent and it is assumed to scale with the agent unimpeded speed v_i^u, as follows:

$$\begin{cases} \sigma_{rf,i} = m_i \cdot \sigma_{ra} \cdot \frac{v_i^u}{v_n} \\ \sigma_{ra} = 0.05 \text{ m/s}^2; \qquad v_n = 1 \text{ m/s} \end{cases} \tag{A.35}$$

The parameter α_F used for the random update of R_F and ϑ_F is selected as being dependent on the relaxation parameter τ_i^f of the motive force of each agent, as follows:

$$\begin{cases} \alpha_{F,i} = \frac{1}{\tau_i^f \cdot k_{\alpha,rf}} \\ k_{\alpha,rf} = 0.2 \end{cases} \tag{A.36}$$

It is worth noting that the selected value of $\alpha_{F,i}$ keeps the aliasing effect to a negligible level with typical time steps used in the simulations, which are of the order of 0.01 s.

The random torque is generated conceptually in the same way as the components of the random force (A.32), but retaining only one term, as follows:

$$T^{\text{rand}} = \cos(\theta_T) \cdot R_T \tag{A.37}$$

with characteristic parameters that are similar to those described in detail for the force, as follows:

$$\begin{cases} \sigma_{rt,i} = I_{z,i} \cdot \sigma_{raa}; \qquad \alpha_{F,i} = \frac{1}{\tau_i^t \cdot k_{\alpha,rt}} \\ \sigma_{raa} = 0.5 \text{ rad/s}^2; \qquad k_{\alpha,rt} = 1 \end{cases} \tag{A.38}$$

The random effects for the counter-flow model are all embedded in the random angle $\delta\psi(t)$ used for changing the orientation of the counter-flow force with respect to its nominal direction, as described before. The angle $\delta\psi(t)$ is directly generated according to the procedure described in this section, using a uniform distribution in $[-\delta\psi_{\text{cf}}, \delta\psi_{\text{cf}}]$ (see Table A.6). The parameter α (see (A.30)) used for the random update of $\delta\psi(t)$ is taken the same as that used for the generation of the random forces (see (A.36)).

A nervousness model has been implemented in the developed tool to model those situations where people tend to get impatient because they cannot achieve the desired target state. The implementation of a nervousness effect can also typically help in overcoming local impasse situations, which could otherwise appear in the simulations, and which cannot be resolved by the effect of random forces alone. The idea of introducing nervousness effects is generally based on the considerations in the work by Helbing et al. [21]. However, it is underlined that the nervousness model presented herein is intended to address the situation where people, while getting impatient, still follow an orderly evacuation process. The model is not intended to be used for representing situations characterised by extreme levels of nervousness leading to panic phenomena, such as those described by Helbing et al. [21].

The general idea to model nervousness is that some parameters of the social forces are instantaneously modified on the basis of the state of the agent in the past. This idea reproduces the fact that people's behaviour is affected not only by instantaneous factors, but also by the short range memory. In particular, the parameters which are affected by nervousness are the relaxation coefficient τ_i^f of the motive force (see (A.5)), the standard deviation $\sigma_{rf,i}$ of the random force (see (A.35)), and the standard deviation $\sigma_{rt,i}$ of the random torque (see (A.38)). While $\tau_i^f(t)$ decreases with respect to the nominal value τ_i^f in case of a situation characterised by nervousness, $\sigma_{rf,i}(t)$ and $\sigma_{rt,i}(t)$, instead, increase with respect to the nominal values $\sigma_{rf,i}$ and $\sigma_{rt,i}$, respectively. To control such variation of parameters, use is made of an instantaneous nervousness parameter $\xi_{\text{inst}}(t)$, defined as follows:

$$\xi_{\text{inst}}\big(v_{i,//}(t), \mathbf{v}_i^0(t)\big) = \begin{cases} \xi_{\max} & \text{for } v_{i,//}(t) < 0 \\ 1.0 & \text{for } v_{i,//}(t) \geqslant v^*(t) \\ \frac{v_{i,//}(t)}{v_i^*(t)} \cdot (1 - \xi_{\max}) + \xi_{\max} & \text{otherwise} \end{cases} \tag{A.39}$$

where $v_{i,//}(t) = \langle \mathbf{v}_i(t), \widehat{\mathbf{v}}_i^0(t) \rangle$ is the component of the instantaneous speed $\mathbf{v}_i(t)$ along the desired speed direction (in this model it is assumed that $\|\mathbf{v}_i^0\| = v_i^0 \neq 0$), and $\xi_{\max}$ is the parameter controlling the level of nervousness effects. This parameter depends on whether the model is eventually used to define $\tau_i^f(t)$, $\sigma_{rf,i}(t)$ or $\sigma_{rt,i}(t)$. From some preliminary calculations in case of IMO test case 4 [32], the value of $\xi_{\max}$ has been tentatively set, for the different cases, as follows:

$$\begin{cases} \text{For } \tau_i^f(t): & \xi_{\max} = 1.25 \\ \text{For } \sigma_{rf,i}(t): & \xi_{\max} = 8.00 \\ \text{For } \sigma_{rt,i}(t): & \xi_{\max} = 8.00 \end{cases} \tag{A.40}$$

The variable $v_i^*(t)$ is calculated as follows:

$$v_i^*(t) = \begin{cases} k_{\text{nerv}} \cdot \frac{t}{\tau_i^f} \cdot v_i^0 & \text{for } 0 \leqslant t < \tau_i^f \\ k_{\text{nerv}} \cdot v_i^0 & \text{for } t \geqslant \tau_i^f \end{cases} \tag{A.41}$$

with $k_{\text{nerv}} = 0.5$. This value of k_{nerv} guarantees that an agent moving from rest in a free field, and having thus speed $v_i(t) = v_i^0 \cdot (1 - \exp(-t/\tau_i^f))$, is not affected by nervousness effects.

In the model presented by Helbing et al. [21], nervousness effects depend only on the instantaneous state. However, in case of evacuation, usually people get nervous when they are forced to maintain a speed which is much lower than their desired one for a relatively long time. This observation indicates that nervousness effects should be linked with the concept of memory. For this reason, a memory model was integrated within the nervousness model. In particular, the nervousness parameter at time t is defined as the average of the instantaneous nervousness parameter ξ_{inst} in a specified past time window, i.e.:

$$\begin{cases} \xi_{\text{nerv}}(t) = 1.0 & \text{for } t = 0 \\ \xi_{\text{nerv}}(t) = \frac{1}{t - t_{\min}} \int_{t_{\min}}^{t} \xi_{\text{inst}}(s)\, ds & \text{for } t > 0 \\ t_{\min} = \max(0, t - T_{\text{mem}}) \end{cases} \tag{A.42}$$

where T_{mem} is the (maximum) length of the temporal window considered for the memory of one agent. Herein, T_{mem} has been tentatively set to 30 s. Eventually, using $\xi_{\text{nerv}}(t)$, the instantaneous values $\tau_i^f(t)$, $\sigma_{rf,i}(t)$ and $\sigma_{rt,i}(t)$ are determined as follows:

$$\begin{cases} \tau_i^f(t) = \tau_i^f / \xi_{\text{nerv},\tau_i^f}(t) \\ \sigma_{rf,i}(t) = \sigma_{rf,i} \cdot \xi_{\text{nerv},\sigma_{rf,i}}(t) \\ \sigma_{rt,i}(t) = \sigma_{rt,i} \cdot \xi_{\text{nerv},\sigma_{rt,i}}(t) \end{cases} \tag{A.43}$$

where the subscripts added to ξ_{nerv} indicate that a different nervousness factor is in principle determined for each variable, although in the present modelling $\xi_{\text{nerv},\sigma_{rf,i}}(t) = \xi_{\text{nerv},\sigma_{rt,i}}(t)$.

A.9. Behaviour on stairs

Stairs are a fundamental element in ship evacuation, as congestions typically appear at the entrances of stairways. An extension of the model is thus required in order to simulate evacuation on stairs. The fundamental characteristic of evacuation on stairs is the reduction of average pedestrian speed, compared to flat terrain, both in ascending and descending direction. With reference to the maritime field,

MSC.1/Circ.1533 [32] provides values for the unimpeded speeds to be taken into account for people ascending and descending stairs when carrying out advanced evacuation analysis. An overview of the state of the art regarding modelling of human behaviour on stairs was reported by Qu et al. [59], who also described a detailed mathematical model, taking into account also stairs steps, to be used in the social force framework.

The model used herein for embedding pedestrian behaviours on stairs is more simplified compared to the one presented by Qu et al. [59], in order to reduce the computational time (in view of real-time applications) and to reduce the need for a too detailed geometrical modelling of the stairs. The present model takes into account the fact that the employed social force modelling is inherently based on a 2-D dynamical description of the agents' motion, while the change in vertical coordinate is taken into account as a purely geometrical constraint. Stairs, in particular, are modelled as inclined planes, i.e. without accounting for the details of steps. Moreover, the geometrical constraint provides a direct link between the speed parallel to the stairs plane and the projected speed on the planar 2-D domain.

In order to simulate the projected 2-D dynamics of the ith agent, it is necessary to know the projected desired speed vector $\mathbf{v}_i^0$. However, the information which is available during the simulation when an agent is on a stair are the modulus $v_i^{03\mathrm{d}}$ of the desired speed, parallel to the stair, and the projected 2-D unit vector $\widehat{\mathbf{v}}_i^0$ of the desired direction. In order to determine $\mathbf{v}_i^0$, given the unit vector $\widehat{\mathbf{n}}$ normal to the stairs plane, the vector $\mathbf{v}_i^{03\mathrm{d}}$ can be firstly obtained as follows:

$$\begin{cases} \hat{\mathbf{v}}_i^{03\mathrm{d}} = \frac{\widehat{\mathbf{v}}_i^0 - \langle \widehat{\mathbf{n}}, \widehat{\mathbf{v}}_i^0 \rangle \cdot \widehat{\mathbf{n}}}{\| \widehat{\mathbf{v}}_i^0 - \langle \widehat{\mathbf{n}}, \widehat{\mathbf{v}}_i^0 \rangle \cdot \widehat{\mathbf{n}} \|} \\ \mathbf{v}_i^{03\mathrm{d}} = \hat{\mathbf{v}}_i^{03\mathrm{d}} \cdot v_i^{03\mathrm{d}} \end{cases} \tag{A.44}$$

afterwards, the 2-D desired speed vector $\mathbf{v}_i^0$ can be obtained by projecting $\mathbf{v}_i^{03\mathrm{d}}$ onto the $xy-$plane, i.e.

$$\mathbf{v}_i^0 = \left(v_{ix}^{03\mathrm{d}}, v_{iy}^{03\mathrm{d}}, 0 \right) \tag{A.45}$$

Of course, the modulus of the two vectors are such that $\| \mathbf{v}_i^0 \| \leqslant \| \mathbf{v}_i^{03d} \|$ and this model assures that an agent having a 2-D desired speed v_i^0 reaches a speed $v_i^{03\mathrm{d}}$ along the stairs.

The speed modulus $v_i^{03\mathrm{d}}$ is instantaneously determined on the basis of the angle γ which is formed by the unit vector $\hat{\mathbf{v}}_i^{03\mathrm{d}}$ with respect to the horizontal plane. Letting the versor of the vertical axis be $\hat{\mathbf{z}}$, it is:

$$\sin(\gamma) = \left\langle \hat{\mathbf{v}}_i^{03\mathrm{d}}, \hat{\mathbf{z}} \right\rangle \tag{A.46}$$

This model allows to define a continuous variation in time of the reference inclination angle γ when the agent moves, possibly in different directions, on the stairs.

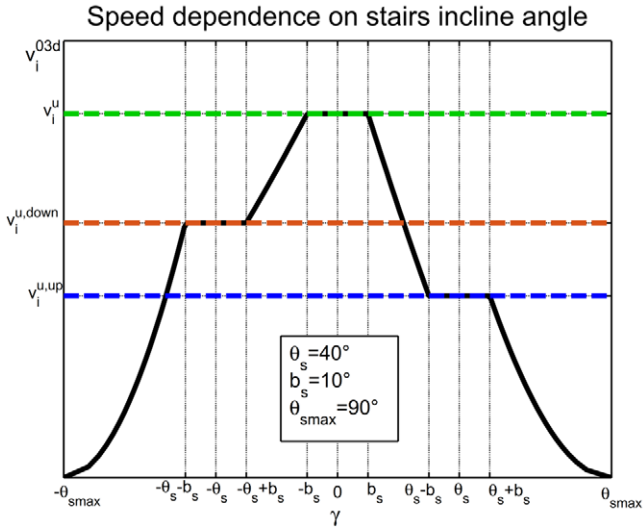

Fig. A.7. Model for the dependence of unimpeded speed v_i^{03d} on the stairs inclination angle γ.

The function used for representing the dependence $v_i^{03d}(\gamma)$ is reported in Fig. A.7, together with an indication of the parameters characterising it. A positive value of γ indicates that the agent is moving upwards, conversely, a negative value of γ indicates a movement downwards. The model assumes that an unimpeded agent moves at a speed v_i^u equal to that on flat terrain whenever the inclination is sufficiently small, in the range $\gamma \in [-b_s, b_s]$. Similarly, the unimpeded agent speed is independent on the inclination angle, with reduced values $v_i^{u,\text{down}}$ and $v_i^{u,\text{up}}$ with respect to v_i^u, in the descending range $\gamma \in [-\theta_s - b_s, -\theta_s + b_s]$ and in the ascending range $\gamma \in [\theta_s - b_s, \theta_s + b_s]$, respectively. The speed is assumed to drop to zero when the inclination reaches $\theta_{s\,\max}$. Intermediate values are obtained by linear interpolation based on $\sin(\gamma)$. The numerical values for the characterising parameters θ_s, b_s and $\theta_{s\,\max}$ are reported in Fig. A.7.

The rationale for the choice of the model and of the parameters is as follows. The desired speed v_i^{03d} is set to the constant value corresponding to the unimpeded speed on flat terrain in the interval $\gamma \in [-10°, 10°]$ as it is reasonable that inclines lower than 10° do not affect the unimpeded speed. Then, specification regarding the speed to be achieved in ascending and descending direction is given in MSC.1/Circ.1533 [32]. In accordance to the FSS Code [34], stairways should not have an incline angle greater than 45° and often the angle ranges from 30° to 45° (see, e.g., the validation data set from SAFEGUARD project [62]). Therefore, the parameters $\theta_s = 40°$ and $b_s = 10°$ have been chosen considering these observations, leading to ranges $\gamma \in [-50°, -30°]$ (descending) and $\gamma \in [30°, 50°]$ (ascending). The unimpeded speed associated with these ranges of inclination values have then been chosen to correspond to the specifications from MSC.1/Circ.1533 [32], in order to guarantee

consistency of simulations in typical layouts. Finally, the parameter $\theta_{s\,\max}$ was set to a maximum possible incline corresponding to 90°, although this was done only for robustness of the model.

The 3-dimensional extension of the model introduces also the problem of the interaction between agents placed at different vertical coordinates. While all the interaction forces are based on the projected 2-D geometry, the effect of the vertical distance d_{vert} between agents is introduced through a separate multiplicative factor $c_{\text{vert}}(d_{\text{vert}})$, which corrects agent-agent, counter-flow and wall-agent interaction forces and torques. The corrective multiplicative factor $c_{\text{vert}}(d_{\text{vert}})$ is described as follows:

$$c_{\text{vert}}(d_{\text{vert}}) = \begin{cases} 1 & \text{if } d_{\text{vert}} < d_{\min} \\ 0 & \text{if } d_{\text{vert}} > d_{\max} \\ \frac{d_{\max} - d_{\text{vert}}}{d_{\max} - d_{\min}} & \text{otherwise} \end{cases} \tag{A.47}$$

where $d_{\min}$ (m) determines the interval $[0, d_{\min}]$ which does not lead to any correction of the forces/torques, whereas $d_{\max}$ (m) determines the maximum vertical distance above which it is assumed that there are no longer interactions. The vertical distance d_{vert} between agents is calculated considering the relative position of agents feet. The value of the characteristic parameters of the model were tentatively set to $d_{\min} = 0.5$ m and $d_{\max} = 1.5$ m.

A.10. Routing

The whole model presented herein is based on the assumption that, at each time step, each agent has a preferred direction $\widehat{\mathbf{v}}_i^0$ that ideally directs the agent to its desired target. The routing problem has herein been addressed by using waypoints and areas, with a logic which is conceptually similar to the one adopted in PTV Vissim [58].

The simulation space is considered to be divided into different areas. A specific facility, connecting two areas, is considered a waypoint. Waypoints are used to model facilities like doors or intersections between corridors, while areas are used to model rooms and corridors. Therefore, the whole map of possible paths can be considered as a graph, where waypoints and areas are nodes and they are considered connected if they are adjacent. A path is therefore described as a list of areas and waypoints. Although in principle such a path could be dynamically modified during the simulation, in the present implementation the agent's path is assigned at the beginning of the evacuation simulation.

However, the representation of waypoints as single target points, is not sufficient to correctly simulate the flow of people through a facility (for example in a bottleneck situation). Therefore, waypoints are represented as convex polygonal regions having some of their sides marked as entrance/exit. An example illustration is depicted in Fig. A.8, where an agent i is positioned in an area A and directed to a waypoint W. Since the left side l of the waypoint W is contained in area A, we say that area A is

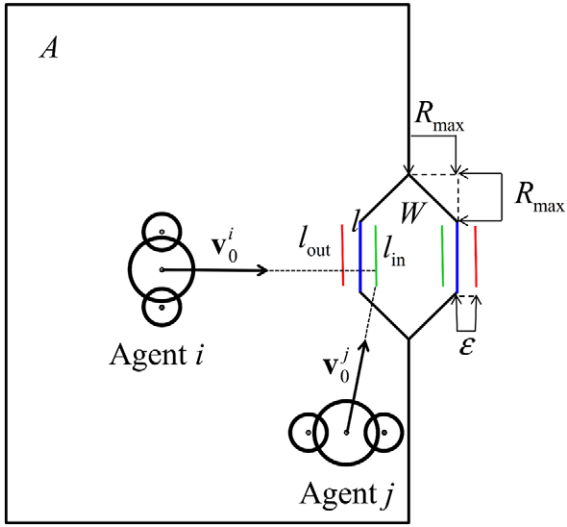

Fig. A.8. Example of routing by means of a waypoint.

connected to W through l. When the side of the waypoint is intended to represent the width of an exit/entrance, its length is set to the effective width, i.e. the clear width reduced by the need for sufficient clearance during the passage of people. Usually, people make an estimation of the effective width of a facility when choosing their direction, taking into account the space occupied by their body. Therefore, an estimation for the clearance can be based on a reasonable global upper bound for the agents radius $R_{\max}$, and the exit/entrance widths are set to the difference between the width of the facility and $2 \cdot R_{\max}$ (Fig. A.8). Moreover, it is reasonable to consider that agents target a point that is not exactly on the facility, but it is instead placed inside the region they occupy and in front of the facility. For these reason hexagonal waypoints regions, as shown in Fig. A.8, have been adopted to represent doors/entrance/exits, while more general shapes can be used in more complex situations. In the typical case of a door, as reported in Fig. A.8, the target point of agent i will be the closest point on the segment l_{in}. The segment l_{in} is obtained by translating l, along its perpendicular, by a distance ε towards the inside of W. Conversely, the segment l_{out} is similarly obtained, but by a translation in the opposite direction, and it is used as target when an agent is inside the waypoint region W and is exiting from it.

The model presented so far does not contain an obstacle avoidance algorithm, since it is assumed that in each situation agents can proceed directly towards the next waypoint. However, in cases of complex geometries with obstacles, this might not be the case. To cope with such situations, a shortest path approach is used. To this end, a triangular mesh of the available area (with holes in correspondence to obstacles) is necessary in addition to the specification of the agent path. The perception of

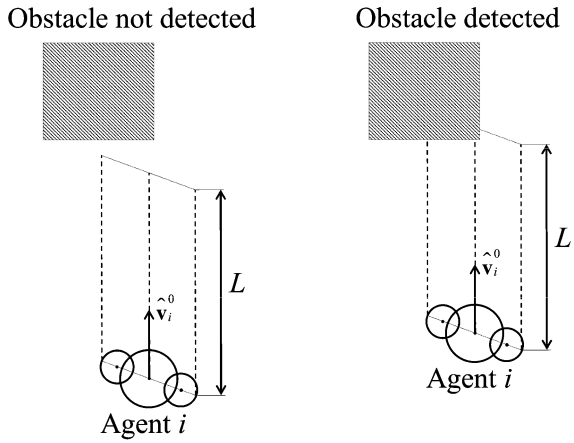

Fig. A.9. Obstacle detection by finite length ray-casting as used for triggering the path-finding algorithm based on shortest path.

Table A.7
Parameters of routing model, and corresponding values

$R_{\max}$	L	ε
0.3 m	3.0 m	0.1 m

obstacles by the agents is based on three rays, with finite length L (which represent the assumed exploration region of the agent), that are cast starting from agents' arms, at half of the height of the agent, parallel to their desired direction $\widehat{\mathbf{v}}_i^0$ (see Fig. A.9). Three rays are used in the algorithm in order to balance the computational effort and the capability of identifying obstacles which are small or which may have complex shapes. In case any of these rays encounters an obstacle, a shortest path algorithm, based on an implementation of the A* algorithm [20], is triggered. The approximate shortest path obtained by connecting the centres of the mesh triangles is subsequently processed with the funnel algorithm, according to the A* Pathfinding Project [16]. However, in the test cases reported later in the paper, there was no need to trigger the path finding algorithm, since waypoints where always visible to agents, without obstacles in between.

Numerical values of the parameters used for the routing model are reported in Table A.7.

A.11. Contacts and collisions

Helbing and Molnar [23] and Korhonen [40] model agent-agent and agent-wall collisions through a force-based spring-damper approach. However, this approach can create numerical integration problems, leading to the need for very small integration time steps, which is problematic in case the target is a real-time simulation.

In the presented model, collisions are instead resolved by the physics engine integrated in the chosen development environment. The physics engine addresses collisions by a direct modification of rigid bodies velocities, and the approach is quite robust also when using relatively large simulation steps. The collision model requires two parameters: the elastic restitution coefficient, that determines the speed after the collision from the speed before the collision, and the friction coefficient for the underlying Coulomb friction model. The elastic restitution coefficient κ_r was tuned from simulations based on FDS+Evac [40] considering the archetypal situation of an agent before and after colliding with a wall. A value $\kappa_r = 0.8$ was eventually set by considering an agent of mass 75 kg, which correspond to the typical human mass used in ship stability calculations. The friction coefficient was set to 0.2. This value is used by Löhner [45] where a Coulomb friction model is implemented.

References

[1] R. Brown, E.R. Galea, S. Deere and L. Filippidis, Passenger response time data-sets for large passenger ferries and cruise ships derived from sea trials, *Transactions of the Royal Institution of Naval Architects, International Journal of Maritime Engineering* **155**(A1) (2013), 33–48.

[2] U. Chattaraj, A. Seyfried and P. Chakroborty, Comparison of pedestrian fundamental diagram across cultures, *Advances in complex systems* **12**(03) (2009), 393–405. doi:10.1142/S0219525909002209.

[3] C.F. Daganzo and N. Geroliminis, An analytical approximation for the macroscopic fundamental diagram of urban traffic, *Transportation Research Part B: Methodological* **42**(9) (2008), 771–781. doi:10.1016/j.trb.2008.06.008.

[4] S.J. Deere, Ship design with the human factor: Evacuation and normal operations modelling in the ship design process, PhD Thesis, University of Greenwich, 2012.

[5] S.J. Deere, E.R. Galea, L. Filippidis and R. Brown, Data collection methodologies used in the SAFEGUARD project to collect human factors data, in: *RINA SAFEGUARD Passenger Evacuation Seminar*, London, UK, 2012, pp. 13–23. doi:10.3940/rina.safe.2012.02.

[6] P. Degond, C. Appert-Rolland, M. Moussaid, J. Pettré and G. Theraulaz, A hierarchy of heuristic-based models of crowd dynamics, *Journal of Statistical Physics* **152**(6) (2013), 1033–1068. doi:10.1007/s10955-013-0805-x.

[7] A. Der Kiureghian and O. Ditlevsen, Aleatory or epistemic? Does it matter?, *Structural Safety* **31**(2) (2009), 105–112. doi:10.1016/j.strusafe.2008.06.020.

[8] M. D'Orazio, L. Spalazzi, E. Quagliarini and G. Bernardini, Agent-based model for earthquake pedestrians' evacuation in urban outdoor scenarios: Behavioural patterns definition and evacuation paths choice, *Safety Science* **62** (2014), 450–465. doi:10.1016/j.ssci.2013.09.014.

[9] D.C. Duives, W. Daamen and S.P. Hoogendoorn, State-of-the-art crowd motion simulation models, *Transportation Research Part C: Emerging Technologies* **37** (2013), 193–209. doi:10.1016/j.trc.2013.02.005.

[10] E.R. Galea, S. Deere, R. Brown and L. Filippidis, An experimental validation of an evacuation model using data sets generated from two large passenger ships, *Journal of Ship Research* **57** (2013), 155–170. doi:10.5957/JOSR.57.3.120037.

[11] E.R. Galea, S. Deere and L. Filippidis, The SAFEGUARD validation data set. A Guide to Data and Validation Procedures – SVGDS2, Fire Safatey Engeneering Group, University of Greenwich, 2012. Available from http://fseg.gre.ac.uk/validation/ship_evacuation.

[12] E.R. Galea, P. Lawrence, S. Gwynne, G. Sharp, N. Hurst, Z. Wang and J. Ewer, Integrated fire and evacuation in maritime environments, in: *Proceedings of the 2nd International Maritime Conference on Design for Safety*, 27–30 October, 2004, Sakai, Japan, 2004, pp. 183–192.

[13] N. Geroliminis and C.F. Daganzo, Existence of urban-scale macroscopic fundamental diagrams: Some experimental findings, *Transportation Research Part B: Methodological* **42**(9) (2008), 759–770. doi:10.1016/j.trb.2008.02.002.
[14] A.I. Ginnis, K.V. Kostas, C.G. Politis and P.D. Kaklis, VELOS: A VR platform for ship-evacuation analysis, *Computer-Aided Design* **42**(11) (2010), 1045–1058. doi:10.1016/j.cad.2009.09.001.
[15] A.I. Ginnis, K.V. Kostas, C.G. Politis and P.D. Kaklis, VELOS-A VR environment for ship applications: Current status and planned extensions, in: *Virtual Realities*, Lecture Notes in Computer Science, Vol. 8844, Springer International Publishing, 2015, pp. 33–55. doi:10.1007/978-3-319-17043-5_3.
[16] A. Granberg, http://arongranberg.com/astar/, Last accessed on 23 November 2021.
[17] L. Guarin, Y. Hifi and D. Vassalos, Passenger ship evacuation – design and verification, in: *Virtual, Augmented and Mixed Reality. Applications of Virtual and Augmented Reality. Part of the Lecture Notes in Computer Science Book Series (LNCS)*, Vol. 8526, Springer International Publishing, 2014, pp. 354–365.
[18] R.Y. Guo, Simulation of spatial and temporal separation of pedestrian counter flow through a bottleneck, *Physica A: Statistical Mechanics and its Applications* **415** (2014), 428–439. doi:10.1016/j.physa.2014.08.036.
[19] S. Ha, N.K. Ku, M.I. Roh and K.Y. Lee, Cell-based evacuation simulation considering human behaviour in a passenger ship, *Ocean Engineering* **53** (2012), 138–152. doi:10.1016/j.oceaneng.2012.05.019.
[20] P.E. Hart, N.J. Nilsson and B. Raphael, A formal basis for the heuristic determination of minimum cost paths, *IEEE transactions on Systems Science and Cybernetics* **4**(2) (1968), 100–107. doi:10.1109/TSSC.1968.300136.
[21] D. Helbing, I. Farkas and T. Vicsek, Simulating dynamical features of escape panic, *Nature* **407**(6803) (2000), 487–490. doi:10.1038/35035023.
[22] D. Helbing, A. Johansson and H.Z. Al-Abideen, Dynamics of crowd disasters: An empirical study, *Physical Review E* **75** (2007), 046109. doi:10.1103/PhysRevE.75.046109.
[23] D. Helbing and P. Molnar, Social force model for pedestrian dynamics, *Physical Review E* **51**(5) (1995), 4282–4286. doi:10.1103/PhysRevE.51.4282.
[24] D. Helbing and A. Johansson, Pedestrian, crowd and evacuation dynamics, in: *Extreme Environmental Events*, R. Meyers, ed., Springer, New York, NY, 2011, pp. 697–716. doi:10.1007/978-1-4419-7695-6_37.
[25] S. Heliövaara, H. Ehtamo, D. Helbing and T. Korhonen, Patient and impatient pedestrians in a spatial game for egress congestion, *Physical Review E* **87**(1) (2013), 012802. doi:10.1103/PhysRevE.87.012802.
[26] S. Heliövaara, T. Korhonen, S. Hostikka and H. Ehtamo, Counterflow model for agent-based simulation of crowd dynamics, *Building and Environment* **48** (2012), 89–100. doi:10.1016/j.buildenv.2011.08.020.
[27] J.C. Helton and D.E. Burmaster, Guest editorial: Treatment of aleatory and epistemic uncertainty in performance assessments for complex systems, *Reliability Engineering & System Safety* **54**(2) (1996), 91–94. doi:10.1016/S0951-8320(96)00066-X.
[28] L.F. Henderson, On the fluid mechanics of human crowd motion, *Transportation Research* **8**(6) (1974), 509–515. doi:10.1016/0041-1647(74)90027-6.
[29] J. Henningsson and J. Blomstrand Martén, Verification and Validation of Viswalk for Building Evacuation Modelling, Report 5481, Department of Fire Safety Engineering, Lund University, 2015. Available from http://lup.lub.lu.se/student-papers/record/5337197.
[30] R.L. Hughes, The flow of human crowds, *Annual review of fluid mechanics* **35**(1) (2003), 169–182. doi:10.1146/annurev.fluid.35.101101.161136.
[31] IMO, *Resolution MSC.404(96) – Amendments to the International Convention for the Safety of Life at Sea, 1974, as Amended*, International Maritime Organization (IMO), London, UK, Adopted on 19 May 2016.

[32] IMO, *MSC.1/Circ.1533 – Revised Guidelines for Evacuation Analysis for New and Existing Passenger Ships*, International Maritime Organization (IMO), London, UK, 6 June 2016.
[33] IMO, SOLAS – International Convention for the Safety of Life at Sea – Consolidated Edition as of 2021, International Maritime Organization, (IMO), London, UK.
[34] IMO, International Code for Fire Safety System (FSS CODE) – Consolidated Edition as of 2021, International Maritime Organization, (IMO), London, UK.
[35] M. Isobe, T. Adachi and T. Nagatani, Experiment and simulation of pedestrian counter flow, *Physica A: Statistical Mechanics and its Applications* **336**(3) (2004), 638–650. doi:10.1016/j.physa.2004.01.043.
[36] Y.Q. Jiang, R.Y. Guo, F.B. Tian and S.G. Zhou, Macroscopic modeling of pedestrian flow based on a second-order predictive dynamic model, *Applied Mathematical Modelling* **40**(23) (2016), 9806–9820. doi:10.1016/j.apm.2016.06.041.
[37] Y.Q. Jiang, P. Zhang, S.C. Wong and R.X. Liu, A higher-order macroscopic model for pedestrian flows, *Physica A: Statistical Mechanics and its Applications* **389**(21) (2010), 4623–4635. doi:10.1016/j.physa.2010.05.003.
[38] A. Johansson, D. Helbing and P.K. Shukla, Specification of the social force pedestrian model by evolutionary adjustment to video tracking data, *Advances in Complex Systems* **10**(supp 02) (2007), 271–288. doi:10.1142/S0219525907001355.
[39] F. Johansson, A. Peterson and A. Tapani, Waiting pedestrians in the social force model, *Physica A: Statistical Mechanics and its Applications* **419** (2015), 95–107. doi:10.1016/j.physa.2014.10.003.
[40] T. Korhonen, Fire Dynamics Simulator with Evacuation: FDS+Evac-Technical Reference and User's Guide (FDS 6.1.0, Evac 2.5.0, DRAFT), 2014, VTT Technical Research Centre of Finland.
[41] T. Korhonen, S. Hostikka, S. Heliövaara and H. Ehtamo, FDS+Evac: An agent based fire evacuation model, in: *Pedestrian and Evacuation Dynamics 2008*, W. Klingsch, C. Rogsch, A. Schadschneider and M. Schreckenberg, eds, Springer, Berlin, Heidelberg, 2010.
[42] T.I. Lakoba, D.J. Kaup and N.M. Finkelstein, Modifications of the Helbing–Molnar–Farkas–Vicsek social force model for pedestrian evolution, *Simulation* **81**(5) (2005), 339–352. doi:10.1177/0037549705052772.
[43] W. Liao, M. Chraibi, A. Seyfried, J. Zhang, X. Zheng and Y. Zhao, Validation of FDS+ Evac for pedestrian simulations in wide bottlenecks, in: *17th International IEEE Conference on Intelligent Transportation Systems (ITSC)*, Qingdao, China, 8–11 October 2014, 2014, pp. 554–559. doi:10.1109/ITSC.2014.6957748.
[44] W. Liao, A. Seyfried, J. Zhang, M. Boltes, X. Zheng and Y. Zhao, Experimental study on pedestrian flow through wide bottleneck, *Transportation Research Procedia* **2** (2014), 26–33. doi:10.1016/j.trpro.2014.09.005.
[45] R. Löhner, On the modeling of pedestrian motion, *Applied Mathematical Modelling* **34**(2) (2010), 366–382. doi:10.1016/j.apm.2009.04.017.
[46] T. Meyer-König, P. Valanto and D. Povel, Implementing ship motion in AENEAS – model development and first results, in: *Pedestrian and Evacuation Dynamics 2005*, Springer, Berlin Heidelberg, 2007, pp. 429–441.
[47] G. Montecchiari, Evacuation dynamics in the maritime field: Modelling, simulation and real-time human participation, PhD Thesis, University of Trieste, XXX Cycle, 2018. http://hdl.handle.net/11368/2920068.
[48] G. Montecchiari, G. Bulian and P. Gallina, Towards real-time human participation in virtual evacuation through a validated simulation tool, *Proceedings of the Institution of Mechanical Engineers, Part O: Journal of Risk and Reliability* **32**(5) (2018), 476–490. doi:10.1177/1748006X17705046.
[49] G. Montecchiari, P. Gallina and G. Bulian, An experiment using immersive virtual reality and a haptic interface to study human behaviour in evacuation, in: *Proc. 27th European Safety and Reliability Conference (ESREL 2017)*, Portoroz, Slovenia, 18–22 June 2017, M. Cepin and R. Bris, eds, Safety and Reliability – Theory and Applications, CRC Press/Balkema, Taylor and Francis Group, Leiden, 2017, pp. 1893–1901.

[50] M. Moussaïd, M. Kapadia, T. Thrash, R.W. Sumner, M. Gross, D. Helbing and C. Hölscher, Crowd behaviour during high-stress evacuations in an immersive virtual environment, *Journal of The Royal Society Interface* **13**(122) (2016), 20160414. doi:10.1098/rsif.2016.0414.
[51] S.Ó. Murphy, K.N. Brown and C. Sreenan, The EvacSim pedestrian evacuation agent model: Development and validation, in: *Proc. 2013 Summer Computer Simulation Conference*, 7–10 July 2013, Toronto, Canada, 2013, pp. 235–242.
[52] NVDIA, http://docs.nvidia.com/gameworks/, Last accessed on 23 November 2021.
[53] A.H. Olivier, J. Bruneau, G. Cirio and J. Pettré, A virtual reality platform to study crowd behaviors, *Transportation Research Procedia* **2** (2014), 114–122. doi:10.1016/j.trpro.2014.09.015.
[54] G. Orosz, R.E. Wilson and G. Stépán, Traffic jams: Dynamics and control, *Philosophical Transactions of the Royal Society A* **368** (2010), 4455–4479. doi:10.1098/rsta.2010.0205.
[55] K.P. Park, S.H. Ham and S. Ha, Validation of advanced evacuation analysis on passenger ships using experimental scenario and data of full-scale evacuation, *Computers in Industry* **71** (2015), 103–115. doi:10.1016/j.compind.2015.03.009.
[56] N. Pelechano, J.M. Allbeck and N.I. Badler, Controlling individual agents in high-density crowd simulation, in: *Proc. 2007 ACM SIGGRAPH/Eurographics Symposium on Computer Animation*, 3–4 August 2007, San Diego, California, 2007, pp. 99–108.
[57] A. Pérez Arias, U.D. Hanebeck, P. Ehrhardt, S. Hengst, T. Kretz, P. Vortisch and P. Vortisch, A framework for evaluating the VISSIM traffic simulation with extended range telepresence, in: *Proc. 22nd Annual Conference on Computer Animation and Social Agents (CASA 2009)*, Amsterdam, Netherlands, 17–19 June 2009, 2009, pp. 13–16.
[58] PTV, *VISSIM 5.30-05 User Manual*. PTV Planung Transport Verkehr AG, Karlsruhe, Germany, 2011.
[59] Y. Qu, Z. Gao, Y. Xiao and X. Li, Modeling the pedestrian's movement and simulating evacuation dynamics on stairs, *Safety Science* **70** (2014), 189–201. doi:10.1016/j.ssci.2014.05.016.
[60] T. Robin, G. Antonini, M. Bierlaire and J. Cruz, Specification, estimation and validation of a pedestrian walking behaviour model, *Transportation Research Part B: Methodological* **43**(1) (2009), 36–56. doi:10.1016/j.trb.2008.06.010.
[61] D. Roggen, M. Wirz, G. Tröster and D. Helbing, Recognition of crowd behaviour from mobile sensors with pattern analysis and graph clustering methods, *Networks and Heterogeneous Media* **6**(3) (2011), 521–544. doi:10.3934/nhm.2011.6.521.
[62] SAFEGUARD, The SAFEGUARD Validation Data Set (SGVDS1, SGVDS2). 3 December 2012.
[63] A. Santos, M. Queirós and G. Montecchiari, Evacuation exercises and simulations toward improving safety at public buildings, in: *From Science to Society. Progress in IS.*, B. Otjacques, P. Hitzelberger, S. Naumann and V. Wohlgemuth, eds, Springer, Cham, 2018, pp. 25–35. doi:10.1007/978-3-319-65687-8_3.
[64] A. Schadschneider, H. Klüpfel, T. Kretz, C. Rogsch and A. Seyfried, Fundamentals of pedestrian and evacuation dynamics, in: *Multi-Agent Systems for Traffic and Transportation Engineering*, A. Bazzan and F. Klügl, eds, IGI Global, 2009, pp. 124–154. doi:10.4018/978-1-60566-226-8.ch006.
[65] S.E. Schaeffer, Graph clustering, *Computer science review* **1**(1) (2007), 27–64. doi:10.1016/j.cosrev.2007.05.001.
[66] J.G. Sørensen and A.S. Dederichs, Evacuation from a complex structure – the effect of neglecting heterogeneous populations, *Transportation Research Procedia* **2** (2014), 792–800. doi:10.1016/j.trpro.2014.09.089.
[67] Unity Technologies, https://unity.com/. Last accessed on 23 November 2021.
[68] O. Tirosh and W.A. Sparrow, Gait termination in young and older adults: Effects of stopping stimulus probability and stimulus delay, *Gait & posture* **19**(3) (2004), 243–251. doi:10.1016/S0966-6362(03)00063-8.
[69] TraffGo-HT, PedEd PedGo PedView AENEASEd AENEASSim AENEASView User Manual. Available at http://www.traffgo-ht.com/downloads/pedestrians/downloads/documents/manual.pdf, Last accessed on 26 November 2021.

[70] D. Vassalos, H.S. Kim, G. Christiansen and J. Majumder, A mesoscopic model for passenger evacuation in a virtual ship-sea environment and performance-based evaluation, in: *Pedestrian and Evacuation Dynamics 2001*, Springer, Netherlands, 2002, pp. 369–391.

[71] H. Vermuyten, J. Beliën, L. De Boeck, G. Reniers and T. Wauters, A review of optimisation models for pedestrian evacuation and design problems, *Safety Science* **87** (2016), 167–178. doi:10.1016/j.ssci.2016.04.001.

[72] N.P. Waterson and E. Pellissier, *The STEPS Pedestrian Microsimulation Tool – a Technical Summary*, Mott MacDonald Limited, Croydon, UK, 6 July 2010.

[73] U. Weidmann, Transporttechnik der Fussgänger, in: *Schriftenreihe des IVT. 90 (Zweite ergänzte Auflage)*, März, ETH Zürich, Zürich, 1993.

[74] H. Xi, S. Lee and Y.J. Son, An integrated pedestrian behaviour model based on extended decision field theory and social force model, in: *Human-in-the-Loop Simulations*, Springer, London, 2011, pp. 69–95. doi:10.1007/978-0-85729-883-6_4.

[75] L. Yang, J. Li and S. Liu, Simulation of pedestrian counter-flow with right-moving preference, *Physica A: Statistical Mechanics and its Applications* **387**(13) (2008), 3281–3289. doi:10.1016/j.physa.2008.01.107.

[76] J. Zhang, Pedestrian fundamental diagrams: Comparative analysis of experiments in different geometries, PhD Thesis, Schriften des Forschungszentrums Jülich, IAS Series, Vol. 14, Universität Wuppertal, 2012. http://hdl.handle.net/2128/4898.

[77] J. Zhang, W. Klingsch, A. Schadschneider and A. Seyfried, Ordering in bidirectional pedestrian flows and its influence on the fundamental diagram, *Journal of Statistical Mechanics: Theory and Experiment* **2012**(02) (2012), P02002. doi:10.1088/1742-5468/2012/02/P02012.

[78] J. Zhang, W. Klingsch, A. Schadschneider and A. Seyfried, Experimental study of pedestrian flow through a T-junction, in: *Traffic and Granular Flow '11*, V. Kozlov, A. Buslaev, A. Bugaev, M. Yashina, A. Schadschneider and M. Schreckenberg, eds, Springer, Berlin, Heidelberg, 2013, pp. 241–249.

[79] X. Zheng, T. Zhong and M. Liu, Modeling crowd evacuation of a building based on seven methodological approaches, *Building and Environment* **44**(3) (2009), 437–445. doi:10.1016/j.buildenv.2008.04.002.